

Ultrafast light-driven optical rotation and hidden orders in bulk WSe₂

Emmanuele Cappelluti,^{1,*} Habib Rostami,^{2,†} and Federico Cilento^{3,‡}

¹*Istituto di Struttura della Materia, CNR (CNR-ISM), 34149 Trieste, Italy*

²*Department of Physics, University of Bath, Claverton Down, Bath BA2 7AY, United Kingdom*

³*Elettra-Sincrotrone Trieste S.C.p.A., 34149 Basovizza, Italy*

Single-layer semiconducting transition-metal dichalcogenides, lacking point inversion symmetry, provide an efficient platform for valleytronics, where the electronic, magnetic, valley and lattice degrees of freedom can be selectively manipulated by using polarized light. This task is however thought to be limited in parent bulk compounds where the point inversion symmetry is restored. Exploiting the underlying quantum physics in bulk materials is thus one of the biggest paradigmatic challenges. Here we show that a sizable optical Kerr rotation can be efficiently generated in a wide energy range on ultrafast timescales in bulk WSe₂, by means of circularly-polarized light. We rationalize these findings as a result of the hidden spin/layer/valley quantum entanglement. The spectral analysis reveals clear features at the three characteristic frequencies corresponding to the A-, B- and C-exciton edges. The origin and the relative sign of all these features is shown to stem from the selective Pauli blocking of intralayer and interlayer optical transitions. The long lifetime of the broadband Kerr response ($\tau \sim 500$ fs) provides a strong indication that coupled photo-induced electron and hole densities survive in bulk compounds longer than previously expected. The present report demonstrates that a hidden quantum entanglement is operative also in bulk centrosymmetric layered materials, opening the way for an effective exploitation of bulk WSe₂ in optoelectronic applications.

Semiconducting members of group-VI transition metal dichalcogenides (TMDs) stand out as highly promising materials for the future of nanotechnology and quantum information [1–3]. These layered materials exhibit a wealth of unique physical properties when manipulated at the single-layer level. Because of the bipartite honeycomb lattice structure and of the lack of inversion symmetry, single-layer TMDs are characterized by a new quantum number, the valley index, with a remarkable entanglement with other inner degrees of freedom (charge, spin, orbital content, ...). The valence bands at the two valleys $\pm K$ are characterized by eigenstates with opposite chiral structure, $|d_{x^2-y^2} \pm i d_{xy}\rangle$, which results in a finite Berry curvature with opposite sign in different valleys,

revealing a non-trivial topological character [1, 4]. Furthermore, the chiral content of the valence bands leads to different sensitivity of different valleys to the light polarization, enforced in valley-dependent optical selection rules [1, 2, 4]. All these features make TMDs an ideal platform for *valleytronics*, i.e. the ability to selectively target a specific valley, and consequently a specific spin, using a tailored optical probe. [5]. This scenario has been widely explored in single-layer TMDs, using a variety of experimental tools, as photoluminescence [6–12], transport [13], angle-resolved photoemission [14] and different optical and magneto-optical probes [2, 15–24]. A common feature of these techniques is the use, as investigation tool, the pump-driven dichroism i.e. the difference of the probe signal between opposite circular polarization of the pump. Bulk TMDs are generally considered less suitable for efficient manipulation of entangled quantum degrees of freedom. Indeed, in bulk 2H-TMD compounds the unit cell contains two layers in an AB structure, which restores inversion symmetry. Consequently, under time-reversal symmetry, valley polarization is not permitted.

Despite this unpromising context, the potential to exploit similar tools in bulk materials for manipulating entangled degrees of freedom remains highly compelling, both from a theoretical perspective and for future market-oriented applications [25]. Recent research has shown that certain internal or *hidden pseudospin* degrees of freedom [26] can indeed be harnessed in bulk materials to restore functional properties at the macroscopic level under equilibrium conditions [26, 27]. Such underlying hidden entanglement has been so far investigated in TMDs mainly by means of angle-resolved photoemission spectroscopy (ARPES), with a specific focus on the spin-polarization of the photo-excited charges in the conduction band, with a spin-dependent dichroism that disappears after very short timescales $t \sim 50-100$ fs [28–32].

Here we show that the optical response of centrosymmetric bulk WSe₂ can be efficiently manipulated in a wide energy range ($\hbar\omega \approx 1.4-2.8$ eV), for a rather longer timescale of ~ 0.5 ps, by using a circularly polarized ultrashort pump pulse, with energy at the A-exciton frequency. Such optical manipulation is revealed by a sizable transient optical Kerr rotation with clear features (and different signs) at the A- and B-exciton energies, as well as at the (high-lying) C-exciton. So far, Kerr rotation was observed only in single-layer TMDs with almost degenerate pump-probe setups, both the pump and the probe energies are set nearly at the same A-exciton resonance. We show that our results on bulk TMDs can be robustly rationalized as a consequence of the hidden en-

* emmanuele.cappelluti@ism.cnr.it

† hr745@bath.ac.uk

‡ federico.cilento@elettra.eu

tanglement between spin, valley, layer and orbital character, this latter ruled by the proper optical selection rules dictated by the Berry curvature. Using a microscopical quantum-field analysis of the optical properties we correctly reproduce the experimental results and identify the origin and the relative signs of the three different features associated to the three different excitonic ranges. The discovery of a relatively long lifetime for the pump-induced Kerr features suggests that in centrosymmetric bulk WSe₂ electron and hole excitations persist in a bound state for significantly longer than previously indicated by ARPES data. The present reports pave the way for an efficient optoelectronic manipulation of quantum degrees of freedom in bulk TMDs, circumventing the limitations about growth and characterization of single-layer systems.

ULTRAFAST KERR ROTATION REVEALED BY TRANSIENT DICHROISM

The bulk semiconducting TMDs with chemical formula MX_2 ($M = \text{Mo, W}$; $X = \text{S, Se}$) share a 2H lattice structure where the unit cell contains two stacked layers MX_2 with a relative rotation of 180 degrees (Fig. 1a). It is known that the interlayer coupling in bulk TMDs changes many of these compounds from direct- to indirect-bandgap semiconductors, with an indirect gap between the Γ and Q points of the Brillouin zone (Fig. 1b) [33, 34]. Despite of this, however, the dominant optical features of bulk systems stem from particle-hole excitations close to the $\pm K$ points, just as for single-layer compounds, and are characterized by two exciton features, termed A and B, which are related, respectively, to the particle-hole excitations between the spin-split upper and lower valence bands and the nearly-degenerate conduction band [33]. Typical values of A and B exciton resonances in bulk WSe₂ at room (low) temperature are $E_A \sim 1.6(1.7)$ eV, $E_B \sim 2.2(2.1)$ eV, respectively, slightly larger than in single-layer compounds [35–37]. Like other TMDs, a further high-energy broad shoulder, usually denoted as “C-exciton”, is reported in WSe₂, which is often associated in literature with band-nesting conditions occurring along the Γ -K path of the Brillouin zone.

In our setup [38], in order to reveal in an efficient way the possible optical Kerr rotation, we perform an experiment (see sketch in Fig. 1c) where a polarization-resolved broadband probe, covering the photon energy range 1.3 – 2.8 eV, is used to detect the pump-induced ultrafast rotation of the optical tensor of a bulk WSe₂ crystal, in a similar way as a Kerr rotation detected in monolayer TMDs under magnetic fields. The WSe₂ crystal is oriented as sketched in Fig. 1a and the probe incoming electric field is fixed oriented at 45 degrees in the x - y plane. The polarization of the out-coming reflectivity is hence detected simultaneously along the horizontal (H) zigzag direction, and along the vertical (V) armchair

direction. Due to such a geometrical configuration, the reflectivity along H- and V-directions is identical under equilibrium conditions. As a pump pulse, we use the laser fundamental at $\hbar\omega_{\text{pump}} = 1.55$ eV, which is nearly-resonant to the first A-exciton state. The pump polarization can be quickly switched between left-circular (LCP) and right-circular (RCP) by means of a liquid-crystal variable waveplate. The incident fluence was set to 500 $\mu\text{J}/\text{cm}^2$. $\Delta R/R$ denotes the normalized differential reflectivity, measured as a function of the pump-probe delay t and the probe photon energy $\hbar\omega$.

Fig. 2a shows one of the four $\Delta R/R$ maps acquired simultaneously, specifically for H probe polarization and RCP pump polarization (the other maps being reported in Extended Data Fig. ED1). Such spectra are sensitive to the broad-frequency effects of the total pump-driven photo-excitations in both valleys from the valence to the conduction bands. Sharp features with negative $\Delta R/R$ at $\hbar\omega = \Delta_A \approx 1.6$ eV and $\hbar\omega = \Delta_B \approx 2.0 - 2.2$ eV signalize the A and B excitonic states, respectively [39]. Here we note an overall predominance of negative $\Delta R/R$, pointing out that such spectral features are governed by a true modification of the optical intensity rather than by an energy shift due to the screening modulation. A clear feature is also detected at $\hbar\omega = \Delta_C \approx 2.6$ eV, at the energy corresponding to the C exciton in bulk WSe₂ [35]. The onset of these features has been rationalized in single-layer TMDs in terms of the combined effect of Pauli blocking and of pump-driven bandgap renormalization [39]. The time scale of the relaxation dynamics of all these features is typically slow ($\sim 34 - 44$ ps, depending on which feature), consistent with previous literature [16, 18, 21, 39–41], and it reflects the fact that the energy gap imposes a bottleneck to the recombination of electrons and holes.

In order to extract the appropriate Kerr signal, we analyze the normalized differential reflectivity $\Delta R/R$ for different circular polarization of the pump photon and for different H/V orientations. The $\Delta R/R$ spectra for these four configurations are shown in Fig. 2b for time delay $t = 200$ fs and $t = 4$ ps, corresponding to vertical grey lines in Fig. 2a. At $t = 4$ ps the normalized differential reflectivity $\Delta R/R$ does not display any sensitivity to the RCP/LCP pump polarization. The observed optical profile of $\Delta R/R$ in this regime can be thus attributed to bandgap renormalization induced by pump-modified electronic screening. We note that $\Delta R/R$ has a slightly different profile along the H/V probe directions. This fact is likely due to a small finite incidence angle ($\lesssim 4^\circ$) of the probe beam, that makes the two polarization states slightly inequivalent. For each given H or V direction, a significant dependence on the circular pump polarization is on the other hand reported at $t = 200$ fs, especially close to each of the three excitonic energies. This is mostly evident close to the A-exciton resonance at $\hbar\omega = 1.6$ eV, where in the V direction RCP gives rise to larger $|\Delta R/R|$ than LCP. The polarization-induced changes in $\Delta R/R$ are reversed along the H direction,

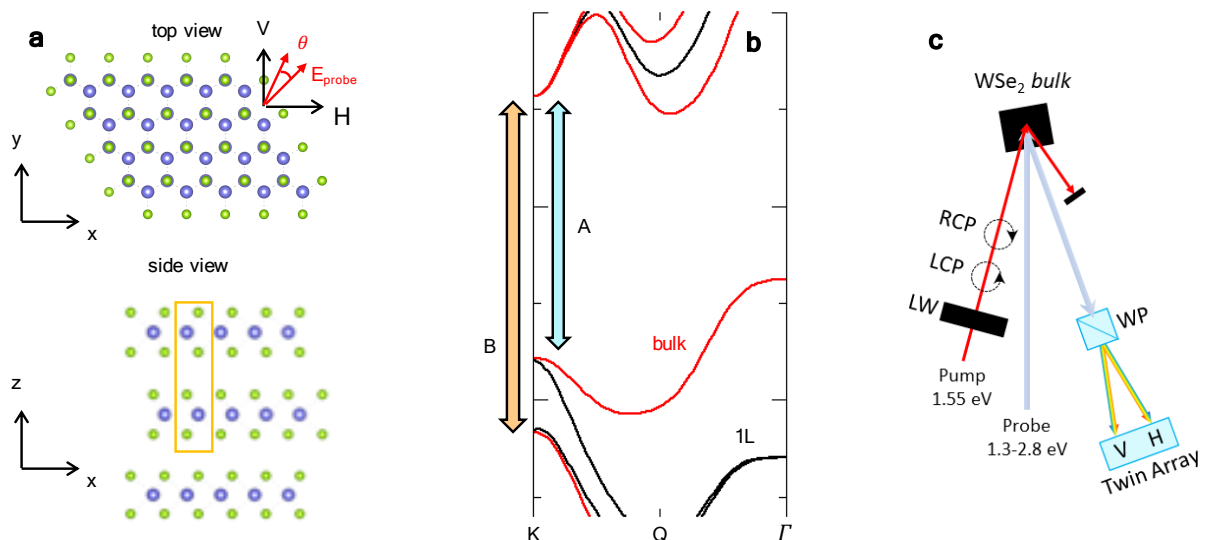


FIG. 1. **Crystal structure, band structure and geometry of the time-resolved experiment.** **a**, Crystal structure of the bulk WSe₂ crystal, from a top view (top panel) and a side view (bottom panel). Tungsten (selenium) atoms are indicated in blue (green). The orange box denotes the bulk unit cell including two WSe₂ layers. Also shown here is the 45° polarization of the incoming probe photon, whereas θ indicates the rotation angle of the polarization of the reflected probe beam. **b**, Schematic band-structure of bulk TMDs (red lines), compared with the band structure of single-layer (black lines). The vertical arrow represents the particle-hole optical transitions responsible for the A- and B-exciton resonances. **c**, Sketch of the experimental configuration: the spectra of the horizontal (H) and vertical (V) components of a broadband supercontinuum beam (1.3 – 2.8 eV), split and dispersed by a Wollaston polarizer (WP), are detected by a twin array detector. The polarization of the pump beam at $\hbar\omega_{\text{pump}} = 1.55$ eV is switched from right-circular (RCP) to left-circular (LCP) by means of a liquid crystal variable waveplate (LW). The probe impinges the sample at near-normal incidence, while the pump impinges at an angle of $\approx 20^\circ$. The bulk WSe₂ crystal is aligned as in panel (a), with its x -axis along the horizontal direction.

with RCP leading in that case to a smaller $|\Delta R/R|$ at $\hbar\omega = 1.6$ eV than LCP, with a reasonably good symmetry. A similar picture is found to be valid in the energy ranges $\hbar\omega \approx 2.2$ eV and $\hbar\omega \approx 2.6$ eV, corresponding to the B and C excitons, although the magnitude of the effect in this case is strongly reduced. Such reversible sensitivity on the circular polarization of the pump cannot be attributed to a pure change of the electronic screening. On the phenomenological ground, the present observations can be recast in terms of a modified optical conductivity tensor σ , with 2×2 components in the x - y space [42]. In the absence of pumping (or at large delay, e.g. $t = 4$ ps), σ is purely diagonal with $\sigma_{xx} = \sigma_{yy}$. The observed pump-driven changes in $\Delta R/R$ can be thus rationalized in terms of a pump-driven onset of an off-diagonal term with $\sigma_{xy} = -\sigma_{yx} \neq 0$, giving rise to a net (Kerr) rotation of the linear probe polarization soon after the photo-excitation, as sketched in the insets of Fig. 2b. The Kerr nature of the observed dichroism is evident from Fig. 2c where we plot the dichroism of $\Delta R/R$ [$\Delta R^*/R = \Delta R/R_{\text{RCP}} - \Delta R/R_{\text{LCP}}$] at $t = 200$ fs along the V and H directions. We note that the energy-shape of $\Delta R^*/R$ along the H probe direction is nicely matched by a corresponding opposite $\Delta R^*/R$ along the V direction. Such analysis is assessed at a quantitative level in the same figure where we further show the sum, $\Delta R^*/R(V) + \Delta R^*/R(H)$, and the

difference, $\Delta R^*/R(V) - \Delta R^*/R(H)$, between the two axes. While the latter quantity can be directly interpreted as a pump-induced Kerr signal, the first one represents what *it is not* Kerr effect. Its negligibility with respect to the Kerr signal, $|\Delta R^*/R(V) + \Delta R^*/R(H)| \ll |\Delta R^*/R(V) - \Delta R^*/R(H)|$, provides thus a robust validation of our results. Equipped with such spectral analysis for bulk WSe₂, we plot in Fig. 2d the energy-time dependence of the optical dichroism $\Delta R^*/R(V) - \Delta R^*/R(H)$ which is proportional to the Kerr angle. For comparison, we performed a similar analysis for bulk WS₂ and MoTe₂ at the same pump energy $\hbar\omega_{\text{pump}} \approx 1.55$ eV (which for these materials is not resonant with the A-exciton), and no trace of any Kerr optical response was found in the whole energy range investigated (see Extended Data Figs. ED2, ED3).

Three important features are worth being pointed out in the data for bulk WSe₂: (i) we show evidence of a sizable optical rotation at *all* the three excitonic frequencies $\hbar\omega \approx 1.6, 2.2, 2.6$ eV, well above the pumping energy $\hbar\omega_{\text{pump}} \approx 1.55$ eV, pointing out that pumping at the A-exciton resonance has a profound impact on the entangled optical properties of all these features in a wide frequency range; (ii) we observe the same sign for the optical dichroism (i.e. Kerr rotation) for both the A and B exciton spectra, but an *opposite* sign for the C-exciton. This can be better visualized in Fig. 2e where

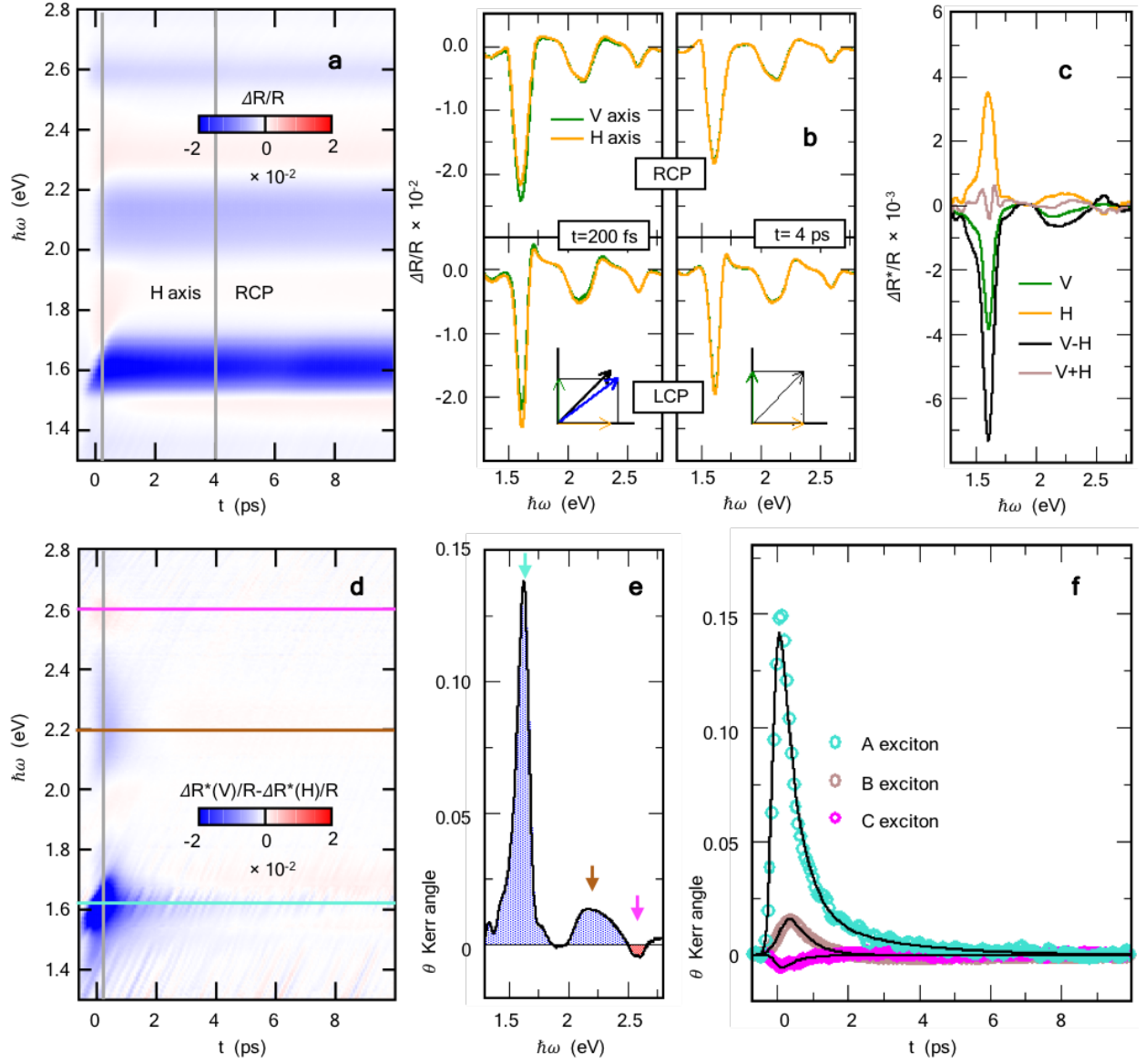


FIG. 2. **Ultrafast pump-driven Kerr rotation in bulk WSe₂.** **a**, Exemplary $\Delta R/R$ map for the H probe component, acquired with RCP pump polarization (the other combinations are reported in Sec. ED1 of the Extended Data), showing typical spectral features for the A, B and C excitons, at energies $\hbar\omega \approx 1.6, 2.2,$ and 2.6 eV. The vertical grey lines at $t = 200$ fs and $t = 4$ ps mark the delays at which the spectral analysis, shown in panel b, has been performed. **b**, Spectral profiles of $\Delta R/R$ for the different combinations of pump and probe polarizations at $t = 200$ fs and $t = 4$ ps. The insets show a sketch of the corresponding rotation of the reflected beam polarization. **c**, Dichroism profiles $\Delta R^*/R$ extracted from panel (b) at $t = 200$ fs along the V and H directions. Also shown are their sum and difference. In particular, the difference signal $\Delta R^*/R(V) - \Delta R^*/R(H)$ is proportional to the optical Kerr rotation angle. The negligible signal $\Delta R^*/R(V) + \Delta R^*/R(H)$ provides a check for the validity of the present analysis. **d**, Energy vs. time color map of the optical dichroism $\Delta R^*/R(V) - \Delta R^*/R(H)$, which is proportional to the rotation angle of the reflected polarization, triggered upon switching the helicity of the pump pulse polarization; **e**, Net Kerr rotation angle θ as a function of the probe photon energy $\hbar\omega$ at $t = 200$ fs (vertical grey line in panel d); **f**, Ultrafast dynamics of the Kerr angle θ at the three representative features (colored symbols corresponding to horizontal cuts in panel d). Also shown are the corresponding fits (black solid lines).

we plot the Kerr angle $\theta(t, \hbar\omega)$ at $t = 200$ fs (vertical line cut in Fig. 2d) as obtained by using the procedure outlined in Ref. 38 (Methods). We characterize each Kerr feature with the energies $\hbar\omega_i = 1.63, 2.2$ and 2.6 eV where its maximum $|\theta^{\max}(t = 200 \text{ fs}, \omega)|$ occurs. The

ratio of the corresponding intensities at $\hbar\omega_i$ ($i = A, B, C$) is found $|\theta_B^{\max}|/|\theta_A^{\max}| \approx 10\%$, $|\theta_C^{\max}|/|\theta_A^{\max}| \approx 3.4\%$. As we will see later, the relative sign among these features can be rationalized and reproduced by means of a microscopical quantum-field analysis, revealing the role

of the valley/spin/layer quantum entanglement and of the interlayer coupling; *(iii)* although the exciton population dynamics is found to decay with a long time-scale $\tau_{\text{long}} \sim 30 - 40$ ps (see Fig. 2a), the optical Kerr rotation at the relevant energies $\hbar\omega_i$ displays much shorter, but still sizable lifetimes. The time evolution of $\theta(t, \hbar\omega_i)$ at the three characteristic energies [horizontal cuts in panel (d)] is shown in Fig. 2f. In order to assess the characteristic timescales of the three features we fit each dataset with a standard fitting procedure, including the pump-probe cross-correlation driven risetime and one or two exponential decays (see the Methods). The fit curves are superimposed as black solid lines over the experimental points in Fig. 2f. We find that the time dynamics of the Kerr angle $\theta(t, \hbar\omega)$ at the A-exciton energy $\hbar\omega = 1.63$ eV cannot be described by a single exponential timescale, whereas a bi-exponential decay $\theta_A(t) \propto a_1 \exp[-t/\tau_{A,\text{fast}}] + a_2 \exp[-t/\tau_{A,\text{slow}}]$ provides a good agreement, with a large component a_1 characterized by a fast dynamics $\tau_{A,\text{fast}} \approx 476 \pm 30$ fs, followed by a weaker component ($a_2/a_1 \approx 0.12$) with a slower dynamics $\tau_{A,\text{slow}} \approx 2315 \pm 50$ fs. The analysis of the time dynamics at the B, C exciton energies displays similar fast timescales with $\tau_B \approx 528 \pm 30$ fs and $\tau_C \approx 511 \pm 30$ fs, while no slower component for these features is detected.

DISCUSSION

The optical Kerr rotation upon circularly polarized pumping implies a time-reversal-symmetry breaking and it has been theoretically predicted and observed in monolayer TMDs [2, 15–21, 23, 24, 43] where it has been attributed to the lack of a center of symmetry, together with the valley-selective population induced by the circularly polarized pumping. To our knowledge, the present observation is the first direct report of a net Kerr effect in *bulk* TMDs with crystal inversion symmetry. The natural questions are then: how a Kerr rotation is activated by circularly-polarized pumping in bulk TMDs without breaking the point-inversion-symmetry? Why similar spectral fingerprints can be found in both (non-centrosymmetric) monolayer and (centrosymmetric) bulk TMDs?

To address these issues, we performed a quantum-field analysis (Methods) of the optical response in the presence of circularly polarized photo-induced particle-hole excitations resonant with the A-exciton energy. In order to capture all the observed Kerr spectral features, we consider a non-interacting model, that is enough to capture the relevant physics, and we employ a six-band $\mathbf{k} \cdot \mathbf{p}$ model that generalizes to the bulk case the three-band model, previously employed for single-layer TMDs [44, 45]. Within this context only relevant d -orbitals of the metal atoms, with atomic orbital angular momentum $l_{\text{at}} = 0, \pm 2$, are retained, providing a good modelling of the relevant valence and conduction bands, as well as of a third block of

bands with $l_{\text{at}} = 2$ d -orbitals, associated with the high-energy excitons and which have been proposed to be responsible for the C-exciton peak. Following previous literature, we assume a local and spin-diagonal spin-orbit coupling [44, 46], and we expand the total Hamiltonian close to the high-symmetry points $\nu\mathbf{K}$ ($\nu = \pm$) of the bulk Brillouin zone, so that $\hat{H}(\mathbf{k}) \approx \sum_{s,\nu} \hat{H}_{s,\nu}(\mathbf{p})$, where $\hat{H}_{s,\nu}$ is defined in the 6×6 orbital space of bulk systems, $s = \pm 1$ is the spin, $\nu = \pm 1$ represents the valley index $\pm\mathbf{K}$, and $\mathbf{p} = \mathbf{k} - \nu\mathbf{K}$ is the relative momentum with respect to the corresponding valley.

Before discussing the full spectral properties of the Kerr response, it is worth clarify the underlying mechanisms giving rise to a finite Kerr rotation. To this purpose we focus for the moment on the static limit of the off-diagonal optical tensor $\sigma_{xy}(\hbar\omega \rightarrow 0)$, where the Kerr response extrapolates smoothly to the Hall rotation. Within this framework, it is known that the term $\sigma_{xy}(0)$ can be conveniently related to the underlying topological properties encoded in the Berry curvature $\Omega_{n,s}(\mathbf{k})$, i.e. $\sigma_{xy} = (e^2/\hbar) \sum_{n,s,\nu} \sum_{\mathbf{p}} \Omega_{n,s,\nu}(\mathbf{p}) f[E_{n,s,\nu}(\mathbf{p})]$, where n is the band index and $f[x]$ the momentum/band population factor that, at equilibrium, corresponds to the thermal Fermi-Dirac distribution. We neglect for the moment the high-energy conduction bands, which play a role only for high-energy spectral features, and we consider the reduced 4×4 Hamiltonian where only the low-energy conduction and valence bands are retained, with an effective interlayer hopping term which mainly couples the valence bands (Methods). Such Hamiltonian has been previously conveniently used to underline the intrinsic entanglement between the valley, the layer and the spin polarization [27], which can conveniently be defined in the orbital/layer space. This approach however cannot be generalized in a straightforward way to the Hall/Kerr response since the Berry curvature is defined in the band-space.

Despite this apparent limitation, in the following we show that in bulk TMDs it is possible to define in a compelling way a layer-projection of the Berry curvature for each band. As detailed in Methods section, this task is made feasible in bulk TMDs due to the layered electronic structure *and* to the specific form of the interlayer coupling which is negligible for the conduction bands. Within this context, using the above Hamiltonian $\hat{H}_{s,\nu}(\mathbf{p})$, we can thus evaluate a layer/spin/valley-resolved Berry curvature $\Omega_{n,s,\nu,\alpha}(\mathbf{p})$, which allows us to compute as well a layer/spin/valley-resolved off-diagonal response $\sigma_{xy,s,\nu,\alpha}$, with $\alpha = \pm 1$ standing for the layer index (Methods). Under equilibrium conditions, we obtain at the valley points $\mathbf{p} = 0$:

$$\sigma_{xy,s,\nu,\alpha}^{\text{eq}} = -\frac{e^2}{\hbar} \left[\tilde{\lambda} (\Omega_A - \Omega_B) s + (\Omega_A + \Omega_B) \nu \alpha \right], \quad (1)$$

where Ω_A is the Berry curvature of the top valence band at the valley point (associated with the A-exciton optical transitions), Ω_B is the Berry curvature of the bottom

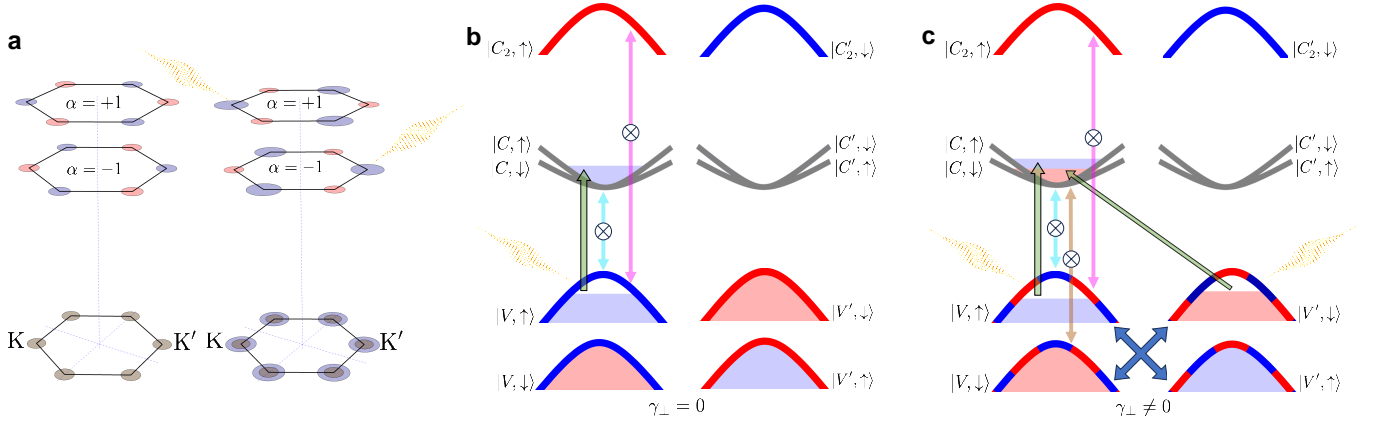


FIG. 3. Hidden order and effects of selection rules on the Kerr optical response. **a**, Schematic representation of the different contributions to the $\sigma_{xy,\alpha,\nu}$ Kerr optical rotation resolved for layer and valleys. For sake of representation, the spin degree has been averaged. The bottom line represent the total layer-averaged $\sigma_{xy,\nu} = \sum_{\alpha} \sigma_{xy,\alpha,\nu}$. Blue/red areas represent the Kerr states resulting in a positive/negative Kerr angle, respectively, while grey areas stand for null Kerr rotation. Left panel shows the hidden order before pumping. LCP laser pumping in the right panel photo-excites charges at K in layer $\alpha = +1$, and at $-K$ in layer $\alpha = -1$. In both cases it results in a net increase of $\sigma_{xy} > 0$ in each valley, resulting in a finite Kerr rotation. The system still obeys inversion symmetry and each valley is equivalent. **b**, Representative selection rules and Pauli-blocked optical transitions at $\nu = 1$ valley in the absence of interlayer coupling. The absorption of a LCP photon tuned at the A-energy triggers particle-hole transitions (upward green arrow) only from the $E_{V,\uparrow}$ state with $l_{\text{at}} = 2$ (blue bands) to $E_{C,\uparrow}$ with $l_{\text{at}} = 0$ (grey bands). The resulting photo-excited charges $n_{V,\uparrow} = n_{C,\uparrow} \neq 0$ induce Pauli blocking (crossed colored vertical double-arrows) at both the A- and C-resonance energies. **c**, Same as panel b in the presence of a finite interlayer coupling, which leads to a mixed l_{at} character for the $E_{V,s}$ bands, resulting in a large charge transfer from $E_{V,\uparrow}$ to $E_{C,\uparrow}$, but also in a finite charge transfer from $E_{V,\downarrow}$ to $E_{C,\downarrow}$, hence $n_{V,\downarrow} = n_{C,\downarrow} \neq 0$. A Pauli-blocking is consequently active also for the particle-hole transitions responsible for the B-resonance.

valence band (associated with the B-exciton optical transitions), and $\tilde{\lambda} = \lambda/\sqrt{\lambda^2 + \gamma_{\perp}^2}$ is a dimensionless parameter expressing the relative relevance of the spin-orbit coupling λ with respect to the interlayer coupling γ_{\perp} . Eq. (1) displays the layer/spin/valley-resolved hidden-order of the Kerr/Hall response. The first term in Eq. (1) descends directly from the analysis of the finite spin-resolved Berry curvature, without the need of a layer-projection, and it reflects the possible onset of a finite Hall/Kerr rotation upon breaking of the time-reversal symmetry [43]. Obeying the space-inversion symmetry, it does not depend on the valley index ν . The second term in Eq. (1) is on the other hand a novel feature which appears only within a layer-resolved analysis and it reveals that in bulk TMDs at equilibrium, although a net (layer-averaged) valley-Hall (valley-Kerr) response is null, a hidden order is present, with a finite valley/layer Hall conductivity response $\sigma_{xy,\nu,\alpha}^{\text{eq}} \neq 0$ as a consequence of the underlying entanglement between valley ν and layer α . A representative plot of the hidden order of $\sigma_{xy,\nu,\alpha}^{\text{eq}}$ is shown in Fig. 3a, showing a staggered pattern in the layer/valley space. Such layer/valley entanglement plays a crucial role in our context since it points out an alternative path for generating a finite Hall/Kerr response in bulk TMDs, not related to a direct time-reversal-symmetry breaking, but as a consequence of a hidden *inversion-symmetry breaking*.

To understand how a circularly-polarized pumping can exploit such hidden order in inducing a finite Kerr rota-

tion, we compute at the valley points ($\mathbf{p} = 0$) the optical selection rules, which can be related to the Berry curvature through the valuable expression [47]:

$$\mathcal{P}_{n \rightarrow m, s, \nu}^{\zeta} = |J_{x, s, \nu}^{nm}(0)|^2 / 2 + |J_{y, s, \nu}^{nm}(0)|^2 / 4 - \zeta [E_{n, s, \nu}(0) - E_{m, s, \nu}(0)]^2 \Omega_{nm, s, \nu}(0) / 4. \quad (2)$$

Eq. (2) is proportional to the probability of absorbing a photon with chiral polarization $\zeta = \pm$ accompanied by a particle-hole excitation from the n -band to the m -band with spin s in the valley ν . On the ground of the above discussion, and as detailed in Methods section, we recognize that the layer indices do not mix in Eq. (2) so that we can properly define *layer-resolved* selection rules $\mathcal{P}_{n \rightarrow m, s, \nu, \alpha}^{\zeta}$ (Methods). Joining $\mathcal{P}_{n \rightarrow m, s, \nu, \alpha}^{\zeta}$ with the detailed expressions of the layer/spin/valley-resolved Berry curvature $\Omega_{n, s, \nu, \alpha}$, we can finally derive the total effect on the off-diagonal optical response of the absorption of a circularly-polarized photon tuned at the A-exciton edge:

$$\delta \bar{\sigma}_{xy, s, \nu, \alpha}^{\zeta} = \delta \sigma_{xy}^{\text{dichro}} \zeta + \delta \sigma_{xy}^{\text{full}} \zeta s \nu \alpha + \delta \sigma_{xy}^{\text{orb}} \nu \alpha + \delta \sigma_{xy}^{\text{spin}} s. \quad (3)$$

The first term in (3) is the only one that survives after averaging over all the internal degrees of freedom, and it is the one responsible for the Kerr response observed in our experimental setup. It arises as consequence of two different channels: the effect of the selection rules of a chiral photon on the spin sector, $\propto \zeta s$, which acts

on top of the spin structure of the hidden order $\propto s$ [first term in Eq. (1)]; and the effect of the selection rules induced by a chiral photon on the orbital order, $\propto \zeta\nu\alpha$, exploiting the underlying hidden order $\propto \nu\alpha$ [second term in Eq. (1)]. A schematic picture of the onset of a finite Hall/Kerr response from such entanglement is shown in the right panel of Fig. 3a: a circularly-polarized photon will act at the $\nu = +1$ valley mainly on layer $\alpha = +1$ and in similar way at $\nu = -1$ on layer $\alpha = -1$. The net result is an off-diagonal term with a well define sign $\delta\sigma_{xy} > 0$ in both valleys, obeying thus the lattice inversion symmetry. The third and fourth terms in (3) on the other hand describe the effects of the pumping that do not give rise to any dichroism, as related for instance to the change of the overall charge distribution. They obey the same symmetries of the bulk system and they follow thus the same pattern of the hidden order. They can be probed in the presence of an explicit space/time breaking by external fields. Finally, the second term of (3) conveys the full entanglement among all the degrees of freedom. The above scenario is consistent with previous ARPES investigations of the hidden valley/helicity/spin entanglement in bulk TMDs [28–32, 48].

After having clarified the mechanisms giving rise to a light-induced Kerr response in centrosymmetric bulk TMDs, we investigate now the fundamental information encoded in the spectral profile of the optical Kerr rotation, with a particular focus on the origin of the three main features outlined in Fig. 2e and on their relative sign. We evaluate the optical conductivity $\sigma_{ij}(\omega)$ ($i, j = x, y$) within a non-interacting Kubo formalism using the full 6×6 Hamiltonian, retaining thus also the high-energy conduction bands. As shown in Methods, three main contributions can be identified, $\sigma_{ij}^A(\omega)$, $\sigma_{ij}^B(\omega)$, $\sigma_{ij}^C(\omega)$, associated with the interband transitions responsible for the A-, B- and C-exciton optical features, respectively. The off-diagonal part of each of these terms fulfills at a spectral level, under equilibrium conditions, the same symmetries as their static limit in Eq. (1), and it vanishes in the absence of symmetry breaking or of external fields.

Finite spectral features $\delta\sigma_{xy}(\omega)$ appear however upon the effect of circularly-polarized pumping tuned at the A-exciton resonance. For standard values of fluence, pump-driven particle-hole excitations are localized very close to valleys $\mathbf{p} = 0$, modifying in a non-thermal way the population factors $f[E_n] \approx f^{\text{eq}}[E_n] + \delta f[E_n]$. The selection rules reported in Eq. (2) provide a useful guidance for evaluating such effects. More in details, we obtain:

$$\mathcal{P}_{V \rightarrow C, s, \nu}^{\zeta}(0) = (1 - \tilde{\lambda}\zeta s - \nu\zeta + \tilde{\lambda}s\nu)/4, \quad (4)$$

$$\mathcal{P}_{V \rightarrow C', s, \nu}^{\zeta}(0) = (1 - \tilde{\lambda}\zeta s + \nu\zeta - \tilde{\lambda}s\nu)/4, \quad (5)$$

where $\mathcal{P}_{V \rightarrow C}^{\zeta}$, $\mathcal{P}_{V \rightarrow C'}^{\zeta}$ describe the probability of transition from the top valence band V to the (degenerate) low-energy conduction bands C, C'. Using such information within the Kubo computation of the off-diagonal optical response, we can estimate the integrated spec-

tral area $I_K^i = \sum_{s, \nu} \int \text{Im} \delta\sigma_{xy, s, \nu}^i(\omega) d\omega$, for each of the optical Kerr features:

$$I_K^A \propto -\frac{v_1^2}{\Delta_A} (1 + 3\tilde{\lambda}^2)\zeta, \quad (6)$$

$$I_K^B \propto -\frac{v_1^2}{\Delta_B} (1 - \tilde{\lambda}^2)\zeta, \quad (7)$$

$$I_K^C \propto \frac{v_3^2}{\Delta_C} \tilde{\lambda}(1 + \tilde{\lambda})\zeta, \quad (8)$$

where the factors v_1, v_3 are related to the current matrix element between different bands.

Noticeable information are encoded in Eqs. (6)-(8): (i) they predict that the Kerr rotation at the A- and B-resonances have the same sign, and an opposite sign with respect to the Kerr rotation at the C-edge, in perfect agreement with the experimental observations; (ii) the onset of a Kerr response at the B-resonance in bulk TMDs under circularly-polarized pumping is intimately related to the interlayer coupling, and it would vanish in the decoupled-layer limit $\tilde{\lambda} \rightarrow 1$; (iii) on the other hand, the spin-orbit coupling has a fundamental role in the Kerr feature at the C-edge, and it would disappear in the opposite limit of no spin-orbit (or extremely large interlayer coupling) $\tilde{\lambda} \rightarrow 0$. On the quantitative level, taking from literature the values of $\tilde{\lambda} = 0.959$, [27] and of the ratio $v_3/v_1 = 0.733$, [45] we estimate $|I_K^A| > |I_K^B| > |I_K^C|$, with $|I_K^B|/|I_K^A| \approx 0.24$ and $|I_K^C|/|I_K^A| \approx 0.16$. Note that such estimates are based on a non-interacting analysis and do not take into account thus many-body renormalization and other effects). More precise first-principle analyses, using GW-BSE calculations, predict for instance a much smaller ratio of the optical oscillation strengths $v_3^2/v_1^2 \approx 0.04$ [11], in even further agreement with the experimental observation.

We can achieve a more microscopical insight on the processes responsible for each spectral feature, and on their time-dynamics, by relating, using the Kubo formalism, the Kerr spectral intensity at different energies to pump-driven photo-excited charge densities $n_{n, s}$. In particular, focusing at a single valley $\nu = 1$ (in bulk systems both valley are equivalent) and for left-circularly-polarized photons, we get:

$$I_K^A(t) \propto \frac{v_1^2}{\Delta_A} [c_\lambda^2(n_{C, \uparrow} - n_{C, \downarrow}) - s_\lambda^2(n_{C', \uparrow} - n_{C', \downarrow}) + (c_\lambda^2 - s_\lambda^2)(n_{V, \uparrow} - n_{V, \downarrow})], \quad (9)$$

$$I_K^B(t) \propto \frac{v_1^2}{\Delta_B} [s_\lambda^2(n_{C, \uparrow} - n_{C', \downarrow}) + c_\lambda^2(n_{C, \downarrow} - n_{C', \uparrow})], \quad (10)$$

$$I_K^C(t) \propto -\frac{v_3^2}{\Delta_C} c_\lambda^2(n_{V, \uparrow} - n_{V, \downarrow}). \quad (11)$$

Here the prefactors $c_\lambda^2 = (1 + \tilde{\lambda})/2$ and $s_\lambda^2 = (1 - \tilde{\lambda})/2$ take into account the (time-independent) magnitude of the optical activities for given interband transitions, whereas the population $n_{n, s}(t)$ can have a time dynamics.

Let us first consider as a template case the limit of decoupled layers $\gamma_\perp = 0$ in the bulk 2H structure. In

that case $c_\lambda^2 = 1$, $s_\lambda^2 = 0$. Keeping in mind that the two layers of the units cell are rotated each other by 180° , the electronic structure of the bulk systems is thus obtained by the degenerate superposition of the electronic states $\psi_n(\mathbf{k}, \alpha = +1)$ and of the electronic states $\psi_n(\mathbf{k}, \alpha = -1)$. In this limit the bulk bands are thus completely layer-localized, with bands of layer $\alpha = +1$ corresponding to the K point of the single-layer system, and bands of layer $\alpha = -1$ corresponding to K' . At $t = 0$ the absorption of a LCP photon with energy tuned at the A-exciton edge $\hbar\omega \approx \Delta_A$ triggers at $\nu = 1$ particle-hole transitions only in layer $\alpha = +1$ (Fig. 3b). Considering also the role of the geometrical phase winding of the Bloch states l_{geo} [7, 49, 50], particle-hole transitions are allowed only from the valence state $E_{V,\uparrow}$, with atomic orbital angular momentum $l_{\text{at}} = 2$ (blue bands) to the conduction state $E_{C,\uparrow}$ with atomic orbital angular momentum $l_{\text{at}} = 0$ (grey bands) [7], with a net total angular momentum change $\Delta l_{\text{tot}} = -1$. The only finite photo-excited charge densities will be thus completely spin-polarized $n_{C,\uparrow} = n_{V,\uparrow} \neq 0$. On the other hand, no particle-hole transitions are allowed from the valence state $E_{V,\downarrow}$ to the conduction band $E_{C',\downarrow}$, although fulfilling the energy-resonant requirement, because $E_{V,\downarrow}$ is localized on the layer $\alpha = -1$ and it borrows from these in-layer states the main orbital angular momentum $l_{\text{at}} = -2$ (red bands) which is not coupled with the absorption of a LCP photon. The concomitant Pauli blocking of the conduction and valence bands, $E_{C,\uparrow}$, $E_{V,\uparrow}$ with a change of the selected orbital angular momentum $\Delta l_{\text{tot}} = -1$, gives rise to the finite Kerr response at the A-edge energy, with an overall spectral area as in Eq. (9). On the other hand, the photo-excited hole density in the valence band $E_{V,\uparrow}$ is responsible also for the Pauli blocking of the optical transitions between the valence band $E_{V,\uparrow}$ and the high-energy conduction band $E_{C_2,\uparrow}$, associated with the C-exciton shoulder. However, due to the different orbital character of conduction bands C_2 ($l_{\text{at}} = 2$) with respect to conduction bands C ($l_{\text{at}} = 0$), such Pauli blocking involves a change of total angular momentum $\Delta l_{\text{tot}} = 1$ *opposite* to the one involved in the A-resonance, and hence a Kerr effect at $\hbar\omega = \Delta_C$ with *opposite sign* than at $\hbar\omega = \Delta_A$. The very experimental observation of a Kerr response at the C-edge, furthermore with the correct sign as predicted by the theory, supports thus the identification of the broad C-exciton feature as induced by a strong band nesting for optical transitions between the valence and the high-energy conduction bands at the valley points.

It is worth noticing here that, within the assumption of no interlayer coupling, no Kerr response at the B-resonance is expected as direct effect of circularly-polarized pumping. A finite Kerr rotation at the B-exciton edge upon circularly-polarized pumping has been reported in single-layer TMDs, where it was explained as an effect of the valley depolarization induced by inter-valley scattering [16, 20, 21]. We rule out this possible explanation of our experimental observation since it will

imply an *opposite* sign of the Kerr angle at $\hbar\omega \approx \Delta_B$ with respect to $\hbar\omega \approx \Delta_A$. Our theoretical analysis [Eq. (7)] shows however that a finite Kerr response at the B-resonance, with the correct sign as experimentally observed, is a direct product the circularly-polarized pumping, even in the absence of many-body scattering processes. The physics describing this effect is mathematically captured in Eq. (10) and it is schematically summarized in Fig. 3c. The fundamental feature to be highlighted here is that the interlayer coupling hybridizes states in different layers with opposite orbital angular momentum. The mixed orbital-angular-momentum character is depicted in Fig. 3c as dashed blue-red bands. The remarkable aspect is that at the valley $\nu = +1$, the photo-induced particle-hole excitations, and the corresponding photo-charges, can occur not only between $E_{V,\uparrow}$ and $E_{C,\uparrow}$ (thick vertical green arrow), but also, with a minor extent, between $E_{V,\downarrow}$ and $E_{C,\downarrow}$ (tiny oblique green arrow). The corresponding photo-induced charges at $t = 0$ can be estimated as $n_{C,\uparrow} = c_\lambda^2$, $n_{C,\downarrow} = s_\lambda^2$, $n_{V,\uparrow} = c_\lambda^2$, $n_{V,\downarrow} = s_\lambda^2$, whereas $n_{C',\uparrow} = n_{C',\downarrow} = 0$. The Kerr response at the B-resonance is thus induced by the two parallel channels: the Pauli blocking of the $E_{V',\uparrow} \leftrightarrow E_{C,\uparrow}$ transitions, driven by the large conduction charge $n_{C,\uparrow}$, but with a small current matrix element s_λ^2 induced by the interlayer coupling; and the Pauli blocking of the $E_{V',\downarrow} \leftrightarrow E_{C,\downarrow}$ transitions, driven by the small conduction charge $n_{C,\downarrow}$, but with a large (mainly intralayer) current matrix element s_λ^2 . Both these channels trigger an angular momentum change $\Delta l_{\text{tot}} = -1$, just at the processes associated with the A-resonance, and induce thus a Kerr response at the B-edge with the same sign as at the A-resonance.

Equipped with Eqs. (9)-(11), having identified the origin and the physical processes for all the three spectral features in the Kerr response, we comment on the observed time-dependence. In order to determine the quantum entanglement between the different degrees of freedom and the optical selection rules, Eqs. (9)-(11) [and (4)-(5)] have been derived using a non-interacting model. Such features are not expected to change where the many-body interactions, and the actual formation of bound excitons are taken into account, with the obvious warning that exciton resonance energies should be considered as inferred from the experiments, including thus the many-body band renormalization and the exciton binding energy. Eqs. (9)-(11) provide thus a useful guidance to rationalize the charge time-dynamics, including the effective time-dependence $n_{n,s}(t)$. Starting from the pump-induced populations at $t = 0$, $n_{C,\uparrow}(0) = n_{V,\uparrow}(0) = c_\lambda^2$, $n_{C,\downarrow} = n_{V,\downarrow} = s_\lambda^2$, $n_{C',\uparrow}(0) = n_{C',\downarrow}(0) = 0$, the overall Kerr response fades out either when spin-flip/layer-flip processes lead to equal spin/layer populations at the valley points (e.g. $n_{V,\uparrow} \approx n_{V,\downarrow}$, $n_{C,\uparrow} \approx n_{C',\uparrow}$); or when, in bulk TMDs, photo-excited charges migrate to other points of the Brillouin zone, forming for instance an excitons. Eqs. (9)-(11) appear thus very powerful since the analysis of the time-dependence of the Kerr response

at the A-, B- and C-edges allows in principle to trace in an independent way the time-dynamics of the conduction (I_K^B) and valence (I_K^C) charges, as well as their joint effect (I_K^A). On this ground, it is strikingly remarkable that all the three Kerr features display a similar time-decay with $\tau_{\text{fast}} \approx 500$ fs (leaving aside the weak long-lived component of the A feature). This observation strongly suggests thus that our set-up, with energy pumping tuned at the A-resonance, does *not* induce free itinerant charges $n_{V,s}$, $n_{C,s}$, $n_{C',s}$ in an independent way in the conduction and valence bands, but it simply affects the total number of available excitons. Photo-induced conduction and valence charges are thus still bound together, with the time-scale $t \lesssim 500$ fs, by the exciton binding energy, and they obey thus the same time dynamics, hampering also the independent migration towards different points of the Brillouin zone. The common decay time that we observe for all the three Kerr features at room temperature is comparable with the reported time-dynamics of the Kerr A-feature in monolayer WSe₂ at room temperature [18, 21, 51], suggesting thus that the observed time-dynamics reveals the time decay due to the spin-flip/layer-flip processes, which are similar as in monolayer systems (note that, due to the 2H stacking, layer-flip processes in bulk TMDs are similar to inter-valley processes in monolayer compounds). Time-resolved angle-resolved photoemission spectroscopy (tr-ARPES) explores on the other hand a different physics, tracing the dynamics of the (unbound) charges left by the photoemission process (in the valence bands or in the pump-populated conduction bands). Not bound in the exciton pairs, these charges can optimize their energy by easily migrating to their own minima in bulk samples (Q-point for conduc-

tion, Γ -point for valence bands), with a much faster dynamics [29, 31, 32, 45, 51]. Our results present thus an additional information and they are thus not incompatible with tr-ARPES data in bulk WSe₂, which report a much shorter time decay ($\tau_{B, \text{ARPES}} \approx 100$ fs) for the dichroism in the conduction bands [29, 31, 32].

In summary, we have reported evidence of a sizable Kerr optical rotation, driven by circularly polarized light, in a wide energy range on bulk WSe₂. The present results show that efficient optical manipulation is affordable not only in single-layer TMDs with broken inversion symmetry, but also in centrosymmetric bulk WSe₂, circumventing the limitation of atomically-thin samples. We rationalize the presence of a pump-induced Kerr effect in centrosymmetry bulk TMDs as a result of the time-reversal-symmetry breaking induced by the circularly-polarized light absorption exploiting the hidden entanglement between the orbital content, valleys and layers. This scenario allows for a finite Kerr rotation in bulk samples without a selective valley population. We also argue that the joint analysis of the spectral intensities of the three Kerr features provides a powerful insight on the dynamics of the photo-excited particle-hole excitations. On this ground our findings suggest that bound excitons can live for a rather long time-scale ($\tau \approx 500$ fs) also in bulk TMDs. Similar dichroism and Kerr effects could be exploited in the bulk structure of other transition metal dichalcogenides such as Mo-based compounds. Furthermore, the known presence of a large spin-orbit coupling in WSe₂ implies that a sizable spin polarization is also possible in bulk TMDs, in agreement thus with the findings of Ref. 32.

-
- [1] Liu, G.-B., Xiao, D., Yao, Y., Xu, X. and Yao, W., *Chem. Soc. Rev.* **44**, 2643 (2015).
- [2] Arora, A., *J. Appl. Phys.* **129**, 120902 (2021).
- [3] Koperski, M., Molas, M.R., Arora, A., Nogajewski, K., Slobodeniuk, A.O., Faugeras, C. and Potemski, M., *Nanophotonics* **6**, 1289 (2017).
- [4] Xiao, D., Liu, G.-B., Feng, W., Xu, X. and Yao, W., *Phys. Rev. Lett.* **108**, 196802 (2012).
- [5] Ashish S. and Suman K.P., *J. Phys. D: Appl. Phys.* **55**, 303003 (2022).
- [6] Mak, K.F., He, K., Shan, J. and Heinz, T.F., *Nat. Nanotech.* **7**, 494 (2012).
- [7] Cao, T., Wang, G., Han, W., Ye, H., Zhu, Ch., Shi, J., Niu, Q., Tan, P., Wang, E., Liu, B. and Feng, J., *Nat. Comm.* **3**, 887 (2012).
- [8] Zeng, H., Dai, J., Yao, W., Xiao, D. and Cui, X., *Nat. Nanotech.* **7**, 490 (2012).
- [9] Kozawa, D., Kumar, R., Carvalho, A., Amara, K.K., Zhao, W., Wang, S., Toh, M., Ribeiro, R.M., Castro Neto, A.H., Matsuda, K. and Eda, G., *Nat. Comm.* **5**, 4543 (2014).
- [10] Lagarde, D., Bouet, L., Marie, X., Zhu, C.R., Liu, B.L., Amand, T., Tan, P.H. and Urbaszek, B., *Phys. Rev. Lett.* **112**, 047401 (2014).
- [11] Lin, K.-Q. et al., , *Nat. Comm.* **12**, 5500 (2021).
- [12] Lin, K.-Q., Ziegler, J.D., Semina, M.A., Mamedov, V.J., Watanabe, K., Taniguchi, T., Bange, S., Chernikov, A., Glazov, M.M. and Lupton, J.M., *Nat. Comm.* **13** (2022).
- [13] Mak, K.F., McGill, K.L., Park, J. and McEuen, P.L., *Science* **344**, 1489 (2014).
- [14] Rostami, H., Volckaert, K., Lanata, N., Mahatha, S.K., Sanders, C.E., Bianchi, M., Lizzit, D., Bignardi, L., Lizzit, S., Miwa, J.A., Balatsky, A.V., Hofmann, Ph. and Ulstrup, S. , *Phys. Rev. B* **100**, 235423 (2019).
- [15] Wang, Q., Ge, S., and Li, X., Qiu, J., Ji, Y., Feng, J. and Sun, D., *ACS Nano* **7**, 11087 (2013).
- [16] Mai, C., Barrette, A., Yu, Y., Semenov, Y.G., Kim, K.W., Cao, L. and Gundogdu, K., *Nano Letters* **14**, 202 (2014).
- [17] Plechinger, G., Nagler, P., Schüller, C. and Korn, T., arXiv:1404.7674 (2014).
- [18] Zhu, C.R., Zhang, K., Glazov, M., Urbaszek, B., Amand, T., Ji, Z.W., Liu, B.L. and Marie, X., *Phys. Rev. B* **90**, 161302 (2014).
- [19] Dal Conte, S., Bottegoni, F., Pogna, E.A.A., De Fazio, D., Ambrogio, S., Bargigia, I., D'Andrea, C., Lombardo,

- A., Bruna, M., Ciccacci, F., Ferrari, A.C., Cerullo, G. and Finazzi, M., *Phys. Rev. B* **92**, 235425 (2015).
- [20] Yang, L., Sinitsyn, N.A., Chen, W., Yuan, J., Zhang, J., Lou, J. and Crooker, S.A., *Nat. Phys.* **11**, 830 (2015).
- [21] Yan, T., Yang, S., Li, D. and Cui, X., *Phys. Rev. B* **95**, 241406 (2017).
- [22] Plechinger, G., Nagler, Ph., Arora, A., Schmidt, R., Chernikov, A., Lupton, J., Bratschitsch, R., Schüller, C. and Korn, T., *Phys. Status Solidi RRL* **11**, 1700131 (2017).
- [23] McCormick, E.J., Newburger, M.J., Luo, Y.K., McCreary, K.M., Singh, S., and Martin, I.B., Cichewicz, E.J., Jonker, B.T. and Kawakami, R.K., *2D Mater.* **5**, 011010 (2017).
- [24] Kiemle, J., and Zimmermann, Ph., Holleitner, A.W. and Kastl, Ch., *Nanophoton.* **9**, 2693 (2020).
- [25] Sun, Z., Martinez, A. and Wang, F., *Nat. Photon.* **10**, 227 (2016).
- [26] Zhang, X., Liu, Q., Luo, J.-W., Freeman, A.J. and Zunger, A., *Nat. Phys.* **10**, 387 (2014).
- [27] Gong, Z., Liu, G.-B., Yu, H., Xiao, D., Cui, X., Xu, X. and Yao, W., *Nat. Comm.* **4**, 2053 (2013).
- [28] Riley, J.M. *et al.*, *Nat. Phys.* **10**, 835 (2014).
- [29] Bertoni, R., Nicholson, C.W., Waldecker, L., Hübener, H., Monney, C., De Giovannini, U., Puppini, M., Hoesch, M., Springate, E., Chapman, R.T., Cacho, C., Wolf, M., Rubio, A. and Ernstorfer, R., *Phys. Rev. Lett.* **117**, 277201 (2016).
- [30] Beaulieu, S., Schusser, J., Dong, S., Schüler, M., Pincelli, T., Dendzik, M., Maklar, J., Neef, A., Ebert, H., Hricovini, K., Wolf, M., Braun, J., Rettig, L., Minár, J. and Ernstorfer, R., *Phys. Rev. Lett.* **125**, 216404 (2020).
- [31] Dong, S. *et al.*, *Nat. Sci.* **1**, e10010 (2021).
- [32] Fanciulli, M., Bresteau, D., Gaudin, J., Dong, S., Géneaux, R., Ruchon, T., Tcherbakoff, O., Minár, J., Heckmann, O., Richter, M.C., Hricovini, K. and Beaulieu, S., *Phys. Rev. Lett.* **131**, 066402 (2023).
- [33] Mak, K.F., Lee, Ch., Hone, J., Shan, J. and Heinz, T.F., *Phys. Rev. Lett.* **105**, 136805 (2010).
- [34] Splendiani, A., Sun, L., Zhang, Y., Li, T., Kim, J., Chim, C.-Y., Galli, G. and Wang, F., *Nano Letters* **10**, 1271 (2010).
- [35] Li, Y., Chernikov, A., Zhang, X., Rigosi, A., Hill, H.M., van der Zande, A.M., Chenet, D.A., Shih, E.-M., Hone, J. and Heinz, T.F., *Phys. Rev. B* **90**, 205422 (2014).
- [36] Arora, A., Koperski, M., Nogajewski, K., Marcus, J., Faugeras, C. and Potemski, M., *Nanoscale* **7**, 10421 (2015).
- [37] Morozov, Y.V. and Kuno, M., *Appl. Phys. Lett.* **107**, 083103 (2015).
- [38] Perlangeli, M., Peli, S., Soranzio, D., Puntel, D., Fulvio Parmigiani, F. and Cilento, F., *Opt. Express* **28**, 8819 (2020).
- [39] Pogna, E.A.A., Marsili, M., De Fazio, D., Dal Conte, S., Manzoni, C., Sangalli, D., Yoon, D., Lombardo, A., Ferrari, A.C., Marini, A., Cerullo, G. and Prezzi, D., *ACS Nano* **10**, 1182 (2016).
- [40] Shi, H., Yan, R., Bertolazzi, S., Brivio, J., Gao, B., Kis, A., Jena, D., Huili, G.X. and Huang, L., *ACS Nano* **7**, 1072 (2013).
- [41] Cui, Q., Ceballos, F., Kumar, N. and Zhao, H., *ACS Nano* **8**, 2970 (2014).
- [42] Levallois, J., Nedoliuk, I.O., Crassee, I. and Kuzmenko, A.B., *Rev. Sci. Instr.* **86**, 033906 (2015).
- [43] Catarina, G., Peres, N.M.R. and Fernández-Rossier, J., *2D Mater.* **7**, 025011 (2020).
- [44] Liu, Gui-Bin and Shan, Wen-Yu and Yao, Yugui and Yao, Wang and Xiao, Di, *Phys. Rev. B* **88**, 085433 (2013).
- [45] Rostami, H., Cilento, F. and Cappelluti, E., *Nanomater.* **14**, 707 (2024).
- [46] Roldán, R., López-Sancho, M.P., Guinea, F., Cappelluti, E., Silva-Guillén, J.A. and Ordejón, P., *2D Mater.* **1**, 034003 (2014).
- [47] Xiao, D., Chang, M.-C. and Niu, Q., *Rev. Mod. Phys.* **82**, 1959 (2010).
- [48] Razzoli, E. *et al.*, *Phys. Rev. Lett.* **118**, 086402 (2017).
- [49] Yao, W., Xiao, D. and Niu, Q., *Phys. Rev. B* **77**, 235406 (2008).
- [50] Rostami, H. and Asgari, R., *Phys. Rev. B* **91**, 075433 (2015).
- [51] Molina-Sánchez, A., Sangalli, D., Wirtz, L. and Marini, A., *Nano Letters* **17**, 4549 (2017).
- [52] Levallois, J., Tran, M. and Kuzmenko, A.B., *Solid State Comm.* **152**, 1294 (2012).
- [53] Cappelluti, E., Roldán, R., Silva-Guillén, J.A., Ordejón, P. and Guinea, F., *Phys. Rev. B* **88**, 075409 (2013).
- [54] Kormányos, A. and Burkard, G. and Gmitra, M. and Fabian, J. and Zólyomi, V. and Drummond, N.D. and Fal'ko, V., *2D Mater.* **2**, 022001 (2015).

METHODS

Samples and Experiments

High quality bulk single-crystals of 2H-WSe₂ were purchased from HQ Graphene. Their in-plane orientation was determined by ex-situ LEED (Low Energy Electron Diffraction) experiments, and the samples were mounted in the optical setup accordingly to this information. TR-OS experiments were performed using the experimental setup described in [38]. Briefly, the output of a Ti:Sapphire regenerative Amplifier (Coherent RegA), delivering 50 fs pulses at 800 nm (1.55 eV) and 250 kHz, is splitted for obtaining pump and probe pulses. A broadband supercontinuum pulse extending in a range 400-1100 nm and linearly-polarized at 45 degrees with respect to the optical table is obtained by focusing 1 μ J/pulse of energy (\approx 250 mW of power) in a 3 mm thick Sapphire window. The reflected beam from the sample is separated in its horizontal (H) and vertical (V) polarization components and spectrally dispersed by a Wollaston Polarizer, and finally detected by a pair of 512-pixels CMOS linear array detectors by Hamamatsu. The pump pulse at 800 nm is polarized circularly with a liquid crystal waveplate from Thorlabs, that allows to quickly (\approx 50 ms) switch between the two circular polarization states. The spot size on the sample amounts to 160 μ m and 50 μ m FWHM for the pump and the probe respectively. The two beams cross at an angle of 20 degrees.

Evaluation of Kerr angle from reflectivity anisotropy

We describe here the procedure employed to estimate the Kerr rotation angle from the measurement of the reflectivity anisotropy upon circularly polarized pumping.

For this task, we essentially followed the scheme nicely described in Refs. 42 and 52.

Using the quantum field theory, we first computed microscopically, as described in the previous Section, the optical conductivity tensor

$$\hat{\sigma}(\omega) = \begin{pmatrix} \sigma_{xx}(\omega) & \sigma_{xy}(\omega) \\ -\sigma_{xy}(\omega) & \sigma_{xx}(\omega) \end{pmatrix}, \quad (12)$$

where we have assumed $\sigma_{yy}(\omega) = \sigma_{xx}(\omega)$, and hence the complex dielectric function $\hat{\epsilon}(\omega)$ through the standard relation $\hat{\epsilon}(\omega) = \epsilon_\infty \hat{I} + 4\pi i \sigma_{xx}(\omega)/\omega$.

In our setup, we shed incoming light at 45 degrees in the x - y plane, thus with the same components $E_x = E_y$. The optical response along the along x (H) and y (V) is governed thus by:

$$\epsilon_V(\omega) = \epsilon_{xx}(\omega) + \epsilon_{xy}(\omega), \quad (13)$$

$$\epsilon_H(\omega) = \epsilon_{xx}(\omega) - \epsilon_{xy}(\omega). \quad (14)$$

The corresponding reflectivity along the two axes was thus determined as:

$$r_\alpha(\omega) = \frac{1 - \sqrt{\epsilon_\alpha(\omega)}}{1 + \sqrt{\epsilon_\alpha(\omega)}}, \quad (15)$$

and the absolute value of the reflectivity as:

$$R_\alpha(\omega) = |r_\alpha(\omega)|^2, \quad (16)$$

where $\alpha = H, V$.

The Kerr angle $\theta(\omega)$ has been eventually computed through the standard formula [38]:

$$\theta(\omega) = \frac{1}{2} \frac{R_H(\omega) - R_V(\omega)}{R_H(\omega) + R_V(\omega)}. \quad (17)$$

Time-dependence fitting procedure

The time-traces have been fitted using the conventional approach, making use of one or two exponential decays of the form $a_i \exp(-t/t_i)$, $i = 1, 2$, where a_i is the amplitude of the exponential component, t_i its the corresponding time-constant and t represents the pump-probe delay. The data have been fitted using Igor Pro and performing the convolution of the above expression with a Gaussian function accounting for the finite temporal resolution of the setup, due to the pump-probe cross correlation. The Gaussian FWHM used is 300 fs, that is mostly determined by the large pump-probe crossing angle.

Quantum field Theory analysis

For a detailed description of the relevant features of bulk TMDs, we generalized for bulk TMDs the three-band $\mathbf{k} \cdot \mathbf{p}$ model, previously employed for single-layer TMDs [44, 45]. Within this context only the relevant d -orbitals of the metal atoms with atomic orbital angular momentum $l_{\text{at}} = 0, \pm 2$ are retained, providing a good modeling of the low-energy conduction bands $E_0(\mathbf{p})$ with dominant $l = 0$ character; of the valence bands $E_B(\mathbf{p})$, which correspond actually at the bottom block of bands with dominant $|l_{\text{at}}| = 2$ character; and of a block of high-energy conduction bands, $E_T(\mathbf{p})$, with

dominant $|l_{\text{at}}| = 2$ character, which are responsible for higher energy optical transitions [11, 12, 45]. Taking into account that the two MX_2 layers of the bulk unit cell have a relative rotation of 180 degrees, a suitable Hilbert space at the valley ν was provided by $\psi_{s,\nu}^\dagger = (\psi_{s,\nu,1}^\dagger, \psi_{s,\nu,-1}^\dagger)$ where

$$\psi_{s,\nu,\alpha}^\dagger = (d_{0,s,\alpha}^\dagger, d_{B,s,\nu,\alpha}^\dagger, d_{T,s,\nu,\alpha}^\dagger). \quad (18)$$

Here $d_{0,s,\alpha}^\dagger$ creates in layer α an electron with spin s in the orbital $d_{3z^2-r^2}$; $d_{B,s,\nu,\alpha}^\dagger$ creates in layer α an electron with spin s and with chiral orbital linear combination $d_{x^2-y^2} + i\nu d_{xy}$; $d_{T,s,\nu,\alpha}^\dagger$ creates in layer α an electron with spin s and with chiral orbital linear combination $d_{x^2-y^2} - i\nu d_{xy}$. In this basis the bulk Hamiltonian reads:

$$\hat{H}_{s,\nu}(\mathbf{p}) = \begin{pmatrix} \hat{h}_{s,\nu}(\mathbf{p}) & \hat{h}_\perp \\ \hat{h}_\perp^\dagger & \hat{h}_{s,-\nu}(\mathbf{p}) \end{pmatrix}, \quad (19)$$

where $\mathbf{p} = \mathbf{k} - \nu K$ is the relative momentum with respect to the valley, and $\hat{h}_{s,\nu}(\mathbf{p})$ is the $\mathbf{k} \cdot \mathbf{p}$ Hamiltonian for the single-layer [45]:

$$\hat{h}_{s,\nu}(\mathbf{p}) = \begin{pmatrix} E_0(p) & \hbar v_1 p_{\nu,-} & \hbar v_2 p_{\nu,+} \\ \hbar v_1 p_{\nu,+} & E_B(p) + \lambda s \nu & \hbar v_3 p_{\nu,-} \\ \hbar v_2 p_{\nu,-} & \hbar v_3 p_{\nu,+} & E_T(p) - \lambda s \nu \end{pmatrix}, \quad (20)$$

with $p_{\nu,\pm} = \nu p_x \pm i p_y$ and λ the spin-orbit coupling. The only (spin-diagonal) interlayer term in \hat{h}_\perp is known to be the coupling γ_\perp between the block of E_B bands. Other interlayer couplings mix E_0 and E_T with the large energy difference [53], and their effect can be neglected. The properties of the bulk system were conveniently investigated in the rotated basis that diagonalizes Eq. (19) at $\mathbf{p} = 0$,

$$\phi_{s,\nu}^\dagger = (d_{C,s,\nu}^\dagger, d_{V,s,\nu}^\dagger, d_{C_2,s,\nu}^\dagger, d_{C',s,\nu}^\dagger, d_{V',s,\nu}^\dagger, d_{C_2',s,\nu}^\dagger), \quad (21)$$

where

$$d_{C,s,\nu} = d_{0,s,1}, \quad (22)$$

$$d_{C',s,\nu} = d_{0,s,-1}, \quad (23)$$

$$d_{V,s,\nu} = \cos \chi_{s,\nu} d_{B,s,\nu,1} + \sin \chi_{s,\nu} d_{B,s,-\nu,-1}, \quad (24)$$

$$d_{V',s,\nu} = -\sin \chi_{s,\nu} d_{B,s,\nu,1} + \cos \chi_{s,\nu} d_{B,s,-\nu,-1}, \quad (25)$$

$$d_{C_2,s,\nu} = d_{T,s,\nu,1}, \quad (26)$$

$$d_{C_2',s,\nu} = d_{T,s,-\nu,-1}. \quad (27)$$

Here $\chi_{s,\nu} = (1/2) \arccos(\tilde{\lambda} \nu s)$, where we defined $\tilde{\lambda} = \lambda / \sqrt{\lambda^2 + \gamma_\perp^2}$. For sake of compactness, we define also $c_{s,\nu} = \cos \chi_{s,\nu}$ and $s_{s,\nu} = \sin \chi_{s,\nu}$. In the basis (21) the Hamiltonian reads:

$$\hat{\mathcal{H}}_{s,\nu}(\mathbf{p}) = \begin{pmatrix} \hat{h}_{s,\nu}(\mathbf{p}) & \hat{h}_\perp \\ \hat{h}_\perp^\dagger & \hat{h}'_{s,\nu}(\mathbf{p}) \end{pmatrix}, \quad (28)$$

where

$$\hat{h}_{s,\nu}(\mathbf{p}) = \begin{pmatrix} E_{C,s,\nu}(p) & \hbar v_1 c_{s,\nu} p_{\nu,-} & \hbar v_2 p_{\nu,+} \\ \hbar v_1 c_{s,\nu} p_{\nu,+} & E_{V,s,\nu}(p) & \hbar v_3 c_{s,\nu} p_{\nu,-} \\ \hbar v_2 p_{\nu,-} & \hbar v_3 c_{s,\nu} p_{\nu,+} & E_{C_2,s,\nu}(p) \end{pmatrix}, \quad (29)$$

$$\hat{h}'_{s,\nu}(\mathbf{p}) = \begin{pmatrix} E_{C',s,\nu}(p) & \hbar v_1 c_{s,\nu} p_{-\nu,-} & \hbar v_2 p_{-\nu,+} \\ \hbar v_1 c_{s,\nu} p_{-\nu,+} & E_{V',s,\nu}(p) & \hbar v_3 c_{s,\nu} p_{-\nu,-} \\ \hbar v_2 p_{-\nu,-} & \hbar v_3 c_{s,\nu} p_{-\nu,+} & E_{C_2',s,\nu}(p) \end{pmatrix} \quad (30)$$

and

$$\hat{h}_\perp = \begin{pmatrix} 0 & \hbar v_1 s_{s,\nu} p_{-\nu,+} & 0 \\ \hbar v_1 s_{s,\nu} p_{-\nu,+} & 0 & \hbar v_3 s_{s,\nu} p_{-\nu,-} \\ 0 & \hbar v_3 s_{s,\nu} p_{-\nu,-} & 0 \end{pmatrix}. \quad (31)$$

The current operators $\hat{J}_{i,s,\nu}(\mathbf{p}) = \partial \hat{\mathcal{H}}_{s,\nu}(\mathbf{p}) / \partial p_i$, can be also promptly derived in the band basis from Eq. (28).

The Hamiltonian in Eq. (28) defines at $\mathbf{p} = 0$ the two split valence bands, $E_{V,s,\nu} = E_B + \sqrt{\lambda^2 + \gamma_\perp^2}$, $E_{V',s,\nu}(0) = E_B - \sqrt{\lambda^2 + \gamma_\perp^2}$, with mixed-layer character. They correspond to the antibonding and bonding interlayer states, respectively. On the other hand, due to the negligible interlayer coupling, the states of the low-energy and high-energy conduction bands, are strongly localized on each layer, in accordance with Eqs. (22)-(27), with $E_{C,s,\nu} = E_{C',s,\nu} = E_0$ being essentially degenerate, while $E_{C_2,s,\nu}$, $E_{C'_2,s,\nu}$ display a sizable spin-orbit splitting, $E_{C_2,s,\nu} = E_T - \lambda s\nu$, $E_{C'_2,s,\nu} = E_T + \lambda s\nu$. The energy differences: $\Delta_A = E_0 - E_V$, $\Delta_B = E_0 - E_{V'}$, $\Delta_C = E_T - \lambda - E_V$, define the edges, in the non-interacting limit, for the particle-hole continuum associated with the A-B- and C-exciton resonances, respectively.

Layer-resolved selection rules and layer/spin/valley/photon entanglement in bulk TMDs - In order to analyze the topological character and the optical selection rules of bulk TMDs we focused on the 4×4 reduced relevant Hilbert space where only the valence and low-energy conduction bands were retained [1, 27, 54], neglecting at this stage the additional high-energy conduction bands.

The Berry curvature for each band was computed as $\Omega_{nm,s,\nu}(\mathbf{p}) = \sum_{m \neq n} \Omega_{nm,s,\nu}(\mathbf{p})$, where [1]

$$\Omega_{nm,s,\nu}(\mathbf{p}) = -2\text{Im} \left[\frac{\langle J_{x,s,\nu}(\mathbf{p}) \rangle_{n,m} \langle J_{y,s,\nu}(\mathbf{p}) \rangle_{m,n}}{[E_{n,s,\nu}(\mathbf{p}) - E_{m,s,\nu}(\mathbf{p})]^2} \right]. \quad (32)$$

Here $\langle J_i \rangle_{n,m}$ is the matrix element of the expectation value of the current operators \hat{J}_i expressed in the band-basis (21), and we have implicitly used the fact that the Hamiltonian (28) is diagonal in both the spin and valley degrees of freedom.

For small pump fluences, the light-induced particle-hole excitations are localized nearby the valley points $\mathbf{p} = 0$, so that the physical properties are well captured by an analysis at $\mathbf{p} = 0$. We got in particular:

$$\Omega_{C,s,\nu}(0) = (\Omega_A + \Omega_B) \nu + \tilde{\lambda} (\Omega_A - \Omega_B) s, \quad (33)$$

$$\Omega_{C',s,\nu}(0) = -(\Omega_A + \Omega_B) \nu + \tilde{\lambda} (\Omega_A - \Omega_B) s, \quad (34)$$

$$\Omega_{V,s,\nu}(0) = -2\tilde{\lambda} \Omega_A s, \quad (35)$$

$$\Omega_{V',s,\nu}(0) = 2\tilde{\lambda} \Omega_B s. \quad (36)$$

where $\Omega_A = \hbar^2 v^2 / \Delta_A^2$ is the Berry curvature associated with the particle-hole transitions responsible for the A-exciton edge, and $\Omega_B = \hbar^2 v^2 / \Delta_B^2$ is the Berry curvature associated with the particle-hole transitions responsible for the B-exciton edge.

Within the same framework, we derive the optical selection rules governing the absorption of a photon with chiral polarization $\zeta = \pm$ driving a particle-hole excitation from the n -band to the m -band [47]:

$$\mathcal{P}_{n \rightarrow m,s,\nu}^\zeta = |J_{x,s,\nu}^{nm}(0)|^2 / 2 + |J_{y,s,\nu}^{nm}(0)|^2 / 4 - \zeta [E_{n,s,\nu}(0) - E_{m,s,\nu}(0)]^2 \Omega_{nm,s,\nu}(0) / 4. \quad (37)$$

In the specific case of a pump energy tuned at the A-exciton edge, i.e. accompanied by a particle-hole excitation from the

valence band V to the conduction band C or C', we get the dimensionless expressions:

$$\mathcal{P}_{V \rightarrow C,s,\nu}^\zeta(0) = (1 - \tilde{\lambda} \zeta s - \nu \zeta + \tilde{\lambda} s \nu) / 4, \quad (38)$$

$$\mathcal{P}_{V \rightarrow C',s,\nu}^\zeta(0) = (1 - \tilde{\lambda} \zeta s + \nu \zeta - \tilde{\lambda} s \nu) / 4. \quad (39)$$

Further insight was gained by splitting the current operators in their layer-projected components, $\hat{J}_{i,s,\nu} = \sum_\alpha \hat{J}_{i,s,\nu,\alpha}$. It should be remarked that, in general, this projection is *not* sufficient for defining *layer-projected* Berry curvatures and *layer-projected* selection rules, since different layer components can mix in Eq. (32). A careful analysis showed however that at $\mathbf{p} = 0$ such mixing does not occur in our case thanks to the layered structure of bulk TMDs and to the reduced effect of the interlayer coupling. We could thus introduce in a compelling way a *layer-resolved* Berry curvature $\Omega_{n,s,\nu,\alpha}(0)$ such that $\Omega_{n,s,\nu}(0) = \sum_\alpha \Omega_{n,s,\nu,\alpha}(0)$. The possibility of defining a layer-resolved Berry curvature allowed us to treat in a compelling way the layer index as an additional quantum degree of freedom and to evaluate *layer-resolved* (as well a spin/valley-resolved) topological properties, selection rules and, in an ultimate analysis, a *layer-resolved* off-diagonal optical response $\sigma_{xy,s,\nu,\alpha}$ through the relation:

$$\sigma_{xy,s,\nu,\alpha} = -\frac{e^2}{\hbar} \sum_{\mathbf{p},n} \Omega_{n,s,\nu,\alpha}(\mathbf{p}) f[E_{n,s,\nu}(\mathbf{p})], \quad (40)$$

where $f[E]$ is the population factor (non necessarily thermal). In order to investigate the entanglement between the different degrees of freedom, since the Berry curvatures are commonly peaked at the valley points, we focus in detail on the contribution at $\mathbf{p} = 0$, where $\sigma_{xy,s,\nu,\alpha} \approx -(e^2/\hbar) \sum_{\mathbf{p},n} \Omega_{n,s,\nu,\alpha}(0) f[E_{n,s,\nu}(0)]$. Using the layer-projected current operators, we obtain:

$$\Omega_{C,s,\nu,\alpha}(0) = \left[(\Omega_A + \Omega_B) \nu + \tilde{\lambda} (\Omega_A - \Omega_B) s \right] \frac{1 + \alpha}{2}, \quad (41)$$

$$\Omega_{C',s,\nu,\alpha}(0) = \left[-(\Omega_A + \Omega_B) \nu + \tilde{\lambda} (\Omega_A - \Omega_B) s \right] \frac{1 - \alpha}{2}, \quad (42)$$

$$\Omega_{V,s,\nu,\alpha}(0) = -\Omega_A \nu \alpha - \tilde{\lambda} \Omega_A s, \quad (43)$$

$$\Omega_{V',s,\nu,\alpha}(0) = -\Omega_B \nu \alpha + \tilde{\lambda} \Omega_B s. \quad (44)$$

Under equilibrium conditions we obtain thus:

$$\sigma_{xy,s,\nu,\alpha}^{\text{eq}} = -(\Omega_A + \Omega_B) \nu \alpha - \tilde{\lambda} (\Omega_A - \Omega_B) s. \quad (45)$$

The pattern of $\sigma_{xy,s,\nu,\alpha}^{\text{eq}}$ is depicted in Fig. 3a and it displays the intrinsic hidden order of the Kerr response including the spin, valley and layer degrees of freedom. For a bulk-sensitive spin-integrated probe, as our setup in the absence of pumping, we get $\sigma_{xy}^{\text{eq}} = \sum_{s,\nu,\alpha} \sigma_{xy,s,\nu,\alpha}^{\text{eq}} = 0$.

The layer-resolved Berry curvature allowed us to derive also the following layer-resolved optical selection rules:

$$\mathcal{P}_{V \rightarrow C,s,\nu,\alpha}^\zeta(0) = (1 - \tilde{\lambda} \zeta s - \nu \zeta + \tilde{\lambda} s \nu)(1 + \alpha) / 8, \quad (46)$$

$$\mathcal{P}_{V \rightarrow C',s,\nu,\alpha}^\zeta(0) = (1 - \tilde{\lambda} \zeta s + \nu \zeta - \tilde{\lambda} s \nu)(1 - \alpha) / 8. \quad (47)$$

On the ground of Eqs. (46)-(47), along with Eqs. (41)-(44), we could furthermore evaluate the additional contribution $\delta \bar{\sigma}_{xy}^\zeta$ to the off-diagonal response induced by the absorption of circularly-polarized pumping. Retaining the explicit dependence of all the degrees of freedom, after a careful analysis we

get:

$$\begin{aligned} \delta\sigma_{xy,s,\nu,\alpha}^{\zeta} \propto & -\frac{2\Omega_A + \Omega_B + \tilde{\lambda}^2(2\Omega_A - \Omega_B)}{4}\zeta \\ & + \frac{2\Omega_A + \Omega_B + \tilde{\lambda}(2\Omega_A - \Omega_B)}{4}\nu\alpha \\ & + \frac{\tilde{\lambda}\Omega_A}{2}s - \tilde{\lambda}\Omega_A\zeta\alpha s\nu. \end{aligned} \quad (48)$$

Optical Kerr response - In order to achieve a detailed understanding of all observed optical Kerr features, it was important to retain all the optically-active bands, as captured by the Hamiltonian (28). In similar way as for single-layer TMDs, we split thus the total response in three interband contributions [45], $\sigma_{xy} = \sigma_{xy}^{v-c} + \sigma_{xy}^{v-c_2} + \sigma_{xy}^{c-c_2}$. The first term σ_{xy}^{v-c} accounts for interband transitions between the block of valence bands ($v=V, V'$) and the block of low-energy conduction bands ($c=C, C'$), and it is responsible for the spectral features at the A-edge and B-edge exciton energies; the second term $\sigma_{xy}^{v-c_2}$ described the interband transitions between the block of valence bands ($v=V, V'$) and the block of high-energy conduction bands ($c_2=C_2, C'_2$). Finally, the third term describes optical transitions between the block of low-energy conduction bands and the block of high-energy conduction bands. This term is Pauli-blocked in semiconducting bulk TMDs at equilibrium. Although these optical features can be activated upon pumping, they don't play a relevant role in the present context and we neglected them.

The term σ_{xy}^{v-c} can be further divided in a contribution arising from the V bands, as resulting in optical features at the A-exciton edge, $\sigma_{xy}^A = \sigma_{xy}^{V-c}$, and in a contribution arising from the V' bands, as resulting in optical features at the B-exciton edge, $\sigma_{xy}^B = \sigma_{xy}^{V'-c}$. In similar way, one can isolate in $\sigma_{xy}^{v-c_2}$ the contribution $\sigma_{xy}^C = \sigma_{xy}^{V-c_2}$ associated with transitions between the V bands and the band C_2, C'_2 with lowest energy (this latter label depends on the valley/spin index). Using Eqs. (28)-(31) and the Kubo formalism, we can thus write:

$$\begin{aligned} \sigma_{xy,s,\nu}^A(\omega) = & -i\nu\frac{e^2v_1^2}{4\pi^2\hbar^2\omega}\left[c_{s,\nu}^2M(EC_{s,\nu}, E_{V,s,\nu}, \omega)\right. \\ & \left.-s_{s,\nu}^2M(EC'_{s,\nu}, E_{V,s,\nu}, \omega)\right], \end{aligned} \quad (49)$$

$$\begin{aligned} \sigma_{xy,s,\nu}^B(\omega) = & -i\nu\frac{e^2v_1^2}{4\pi^2\hbar^2\omega}\left[s_{s,\nu}^2M(EC_{s,\nu}, E_{V',s,\nu}, \omega)\right. \\ & \left.-c_{s,\nu}^2M(EC'_{s,\nu}, E_{V',s,\nu}, \omega)\right], \end{aligned} \quad (50)$$

$$\begin{aligned} \sigma_{xy,s,\nu}^C(\omega) = & i\nu\frac{e^2v_3^2}{4\pi^2\hbar^2\omega}\left[I_{s\nu}c_{s,\nu}^2M(EC_{2,s,\nu}, E_{V,s,\nu}, \omega)\right. \\ & \left.-I_{-s\nu}s_{s,\nu}^2M(EC'_{2,s,\nu}, E_{V,s,\nu}, \omega)\right], \end{aligned} \quad (51)$$

where

$$\begin{aligned} M(E_n, E_m, \omega) = & \sum_{\mathbf{p}} \left\{ \frac{f[E_n(\mathbf{p})] - f[E_m(\mathbf{p})]}{E_n(\mathbf{p}) - E_m(\mathbf{p}) - \hbar\omega - i\delta} \right. \\ & \left. - \frac{f[E_n(\mathbf{p})] - f[E_m(\mathbf{p})]}{E_n(\mathbf{p}) - E_m(\mathbf{p}) + \hbar\omega + i\delta} \right\}, \end{aligned} \quad (52)$$

and where $I_{s\nu} = (1 + s\nu)/2$ traces down that the level $E_T - \lambda$ is associated with different bands C_2, C'_2 for different valley/spin indices. In semiconducting bulk TMDs at equilibrium, $f[E_{V,s,\nu}(\mathbf{p})] = 1$, $f[EC_{s,\nu}(\mathbf{p})] = 0$, $f[EC_{2,s,\nu}(\mathbf{p})] = 0$, and all the three features vanish once summed over the spin.

Finite spectral features $\delta\sigma_{xy}(\omega)$ appear however upon the effect of circularly-polarized pumping tuned at the A-exciton resonance. For standard values of fluence, pump-driven particle-hole excitation are localized very close to valleys $\mathbf{p} = 0$, modifying in a non-thermal way the population factors $f[E] \approx f^{\text{eq}}[E] + \delta f[E]$. For energies $\hbar\omega$ close to the resonance edge, we could evaluate the change in the response functions:

$$\begin{aligned} \text{Im}\delta M(E_1, E_2, \omega) \approx & \pi\delta[E_1(0) - E_2(0) - \hbar\omega] \\ & \times \sum_{\mathbf{p}} \{\delta f[E_1(\mathbf{p})] - \delta f[E_2(\mathbf{p})]\} \\ = & \pi\delta[E_1(0) - E_2(0) - \hbar\omega] \{\delta n_1 - \delta n_2\}, \end{aligned} \quad (53)$$

where δn_i is the pump-driven charge variation in the corresponding band E_i . Using the selection rules Eqs. (38)-(39) we can estimate $\delta n_{V,s,\nu} = -(1 - \tilde{\lambda}\zeta s)F/2$, $\delta n_{C,s,\nu} = (1 - \tilde{\lambda}\zeta s - \nu\zeta + \tilde{\lambda}s\nu)F/4$, $\delta n_{C',s,\nu} = (1 - \tilde{\lambda}\zeta s + \nu\zeta - \tilde{\lambda}s\nu)F/4$, where F is a factor which scales linearly with the pump fluence. For all the other bands, not affected by a pumping at the A-resonance, $\delta n = 0$. With such modeling we could evaluate thus the pump-driven off-diagonal part the optical tensor, $\delta\sigma_{xy,s,\nu}(\omega)$, and the spectral integrated area of each optical Kerr feature $i=A, B, C$ as

$$I_K^i = \sum_{s,\nu} \int \text{Im} \delta\sigma_{xy,s,\nu}^i(\omega) d\omega. \quad (54)$$

We get:

$$I_K^A \propto -\frac{v_1^2}{\Delta_A}(1 + 3\tilde{\lambda}^2)\zeta F, \quad (55)$$

$$I_K^B \propto -\frac{v_1^2}{\Delta_B}(1 - \tilde{\lambda}^2)\zeta F, \quad (56)$$

$$I_K^C \propto \frac{v_3^2}{\Delta_C}\tilde{\lambda}(1 + \tilde{\lambda})\zeta F. \quad (57)$$

Using the layer-resolved analysis, we computed also the different spin/layer contributions to Eqs. (55)-(57). Focusing on $\nu = 1$, and considering for instance a left-circularly-polarized photon $\zeta = -1$, we get:

$$I_{s,\alpha=1}^A \propto \frac{v_1^2}{\Delta_A} \left(\frac{1 + \tilde{\lambda}^2}{2} + \tilde{\lambda}s \right) F, \quad (58)$$

$$I_{s,\alpha=-1}^A \propto -\frac{v_1^2}{\Delta_A} \left(\frac{1 - \tilde{\lambda}^2}{4} \right) F, \quad (59)$$

$$I_{s,\alpha=1}^B \propto \frac{v_1^2}{\Delta_B} \frac{1 - \tilde{\lambda}^2}{4} F, \quad (60)$$

$$I_{s,\alpha=-1}^B \propto 0, \quad (61)$$

$$I_{s,\alpha=1}^C \propto -\frac{v_3^2}{\Delta_C} \frac{(1 + \tilde{\lambda})^2(1 + s)}{8} F, \quad (62)$$

$$I_{s,\alpha=-1}^C \propto \frac{v_3^2}{\Delta_C} \frac{(1 - \tilde{\lambda})^2(1 - s)}{8} F. \quad (63)$$

Few interesting properties can be noticed here: (i) the Kerr spectral features at the C-resonance $\hbar\omega = \Delta_C$ arises from a unique spin sector, and they are expected to be fully polarized. On the contrary, the Kerr feature at the B-edge $\hbar\omega = \Delta_B$ is totally spin-independent; (ii) the Kerr features at the B-edge stem also from a unique layer; (iii) in the regime of weak interlayer coupling (which is realized in many bulk

TMDs) the Kerr features at the A-resonance $\hbar\omega = \Delta_A$, as well as the C-one, are fully spin and layer polarized. Eq. (53) allowed us to relate the Kerr spectral intensity at different energies to pump-driven photo-excited charge densities. In particular, focusing at a single valley $\nu = 1$, and for left-circularly-polarized photons, we get:

$$I_K^A \propto \frac{v_1^2}{\Delta_A} [c_\lambda^2(n_{C,\uparrow} - n_{C',\downarrow}) - s_\lambda^2(n_{C',\uparrow} - n_{C,\downarrow}) + (c_\lambda^2 - s_\lambda^2)(n_{V,\uparrow} - n_{V,\downarrow})], \quad (64)$$

$$I_K^B \propto \frac{v_1^2}{\Delta_B} [s_\lambda^2(n_{C,\uparrow} - n_{C',\downarrow}) + c_\lambda^2(n_{C,\downarrow} - n_{C',\uparrow})], \quad (65)$$

$$I_K^C \propto -\frac{v_3^2}{\Delta_C} c_\lambda^2(n_{V,\uparrow} - n_{V,\downarrow}), \quad (66)$$

where $c_\lambda^2 = (1 + \tilde{\lambda})/2$ and $s_\lambda^2 = (1 - \tilde{\lambda})/2$.

ACKNOWLEDGEMENTS

E.C. acknowledges financial support from PNRR MUR Project No. PE0000023-NQSTI.

AUTHOR CONTRIBUTIONS STATEMENT

F.C. conceived and conducted the experiments. E.C. and H.R. developed the theory. All the authors conceived the paper and contributed equally to the writing of the manuscript.

COMPETING INTERESTS

The authors declare no competing interests.

ADDITIONAL INFORMATION

Correspondence and requests for materials can be equally addressed to any of the Authors.

Extended Data for: Ultrafast light-driven optical rotation and hidden orders in bulk WSe₂

Emmanuele Cappelluti,^{1,*} Habib Rostami,^{2,†} and Federico Cilento^{3,‡}

¹*Istituto di Struttura della Materia, CNR (CNR-ISM), 34149 Trieste, Italy*

²*Department of Physics, University of Bath, Claverton Down, Bath BA2 7AY, United Kingdom*

³*Elettra-Sincrotrone Trieste S.C.p.A., 34149 Basovizza, Italy*

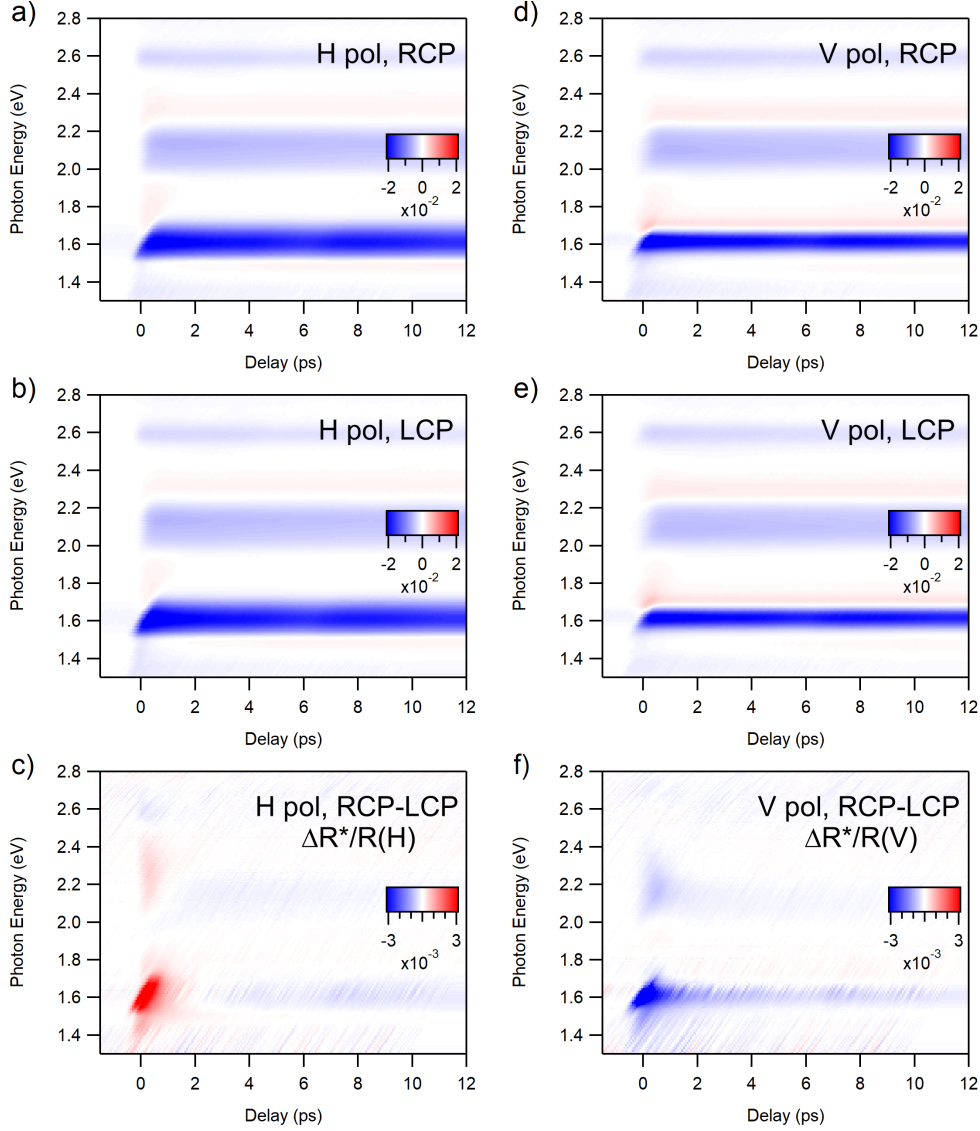


FIG. ED1. Differential reflectivity maps $\Delta R/R$ for bulk 2H-WSe₂ with pump photon energy at $\omega_{\text{pump}} = 1.55$ eV. Panels (a)-(b) show $\Delta R/R$ along the H direction for RCP and LCP, respectively, while panel (c) shows the dichroism $\Delta R^*/R (= \Delta R/R_{\text{RCP}} - \Delta R/R_{\text{LCP}})$. Panels (d)-(f): as in panel (a)-(c) but along the V direction. The remarkable dichroism in both the H and V directions points out the evidence of a relevant Kerr rotation.

* emmanuele.cappelluti@ism.cnr.it

† hr745@bath.ac.uk

‡ federico.cilento@elettra.eu

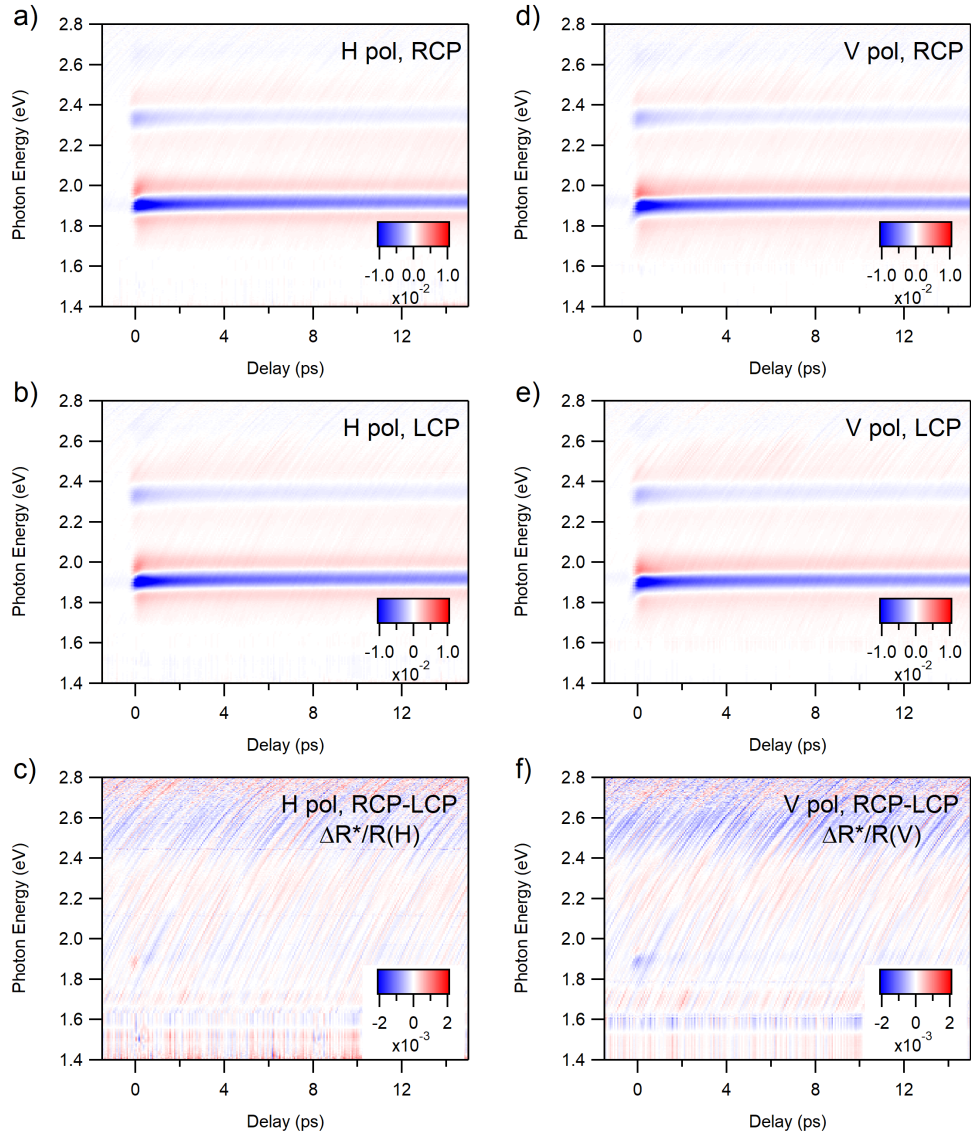


FIG. ED2. Differential reflectivity maps $\Delta R/R$ for bulk 2H-WS₂ with pump photon energy at $\omega_{\text{pump}} = 1.55$ eV. Panels (a)-(b) show $\Delta R/R$ along the H direction for RCP and LCP, respectively, while panel (c) shows the dichroism $\Delta R^*/R = \Delta R/R_{\text{RCP}} - \Delta R/R_{\text{LCP}}$. Panels (d)-(f): as in panel (a)-(c) but along the V direction. The lack of dichroism in both the H and V directions point out the absence of Kerr rotation under these circumstances.

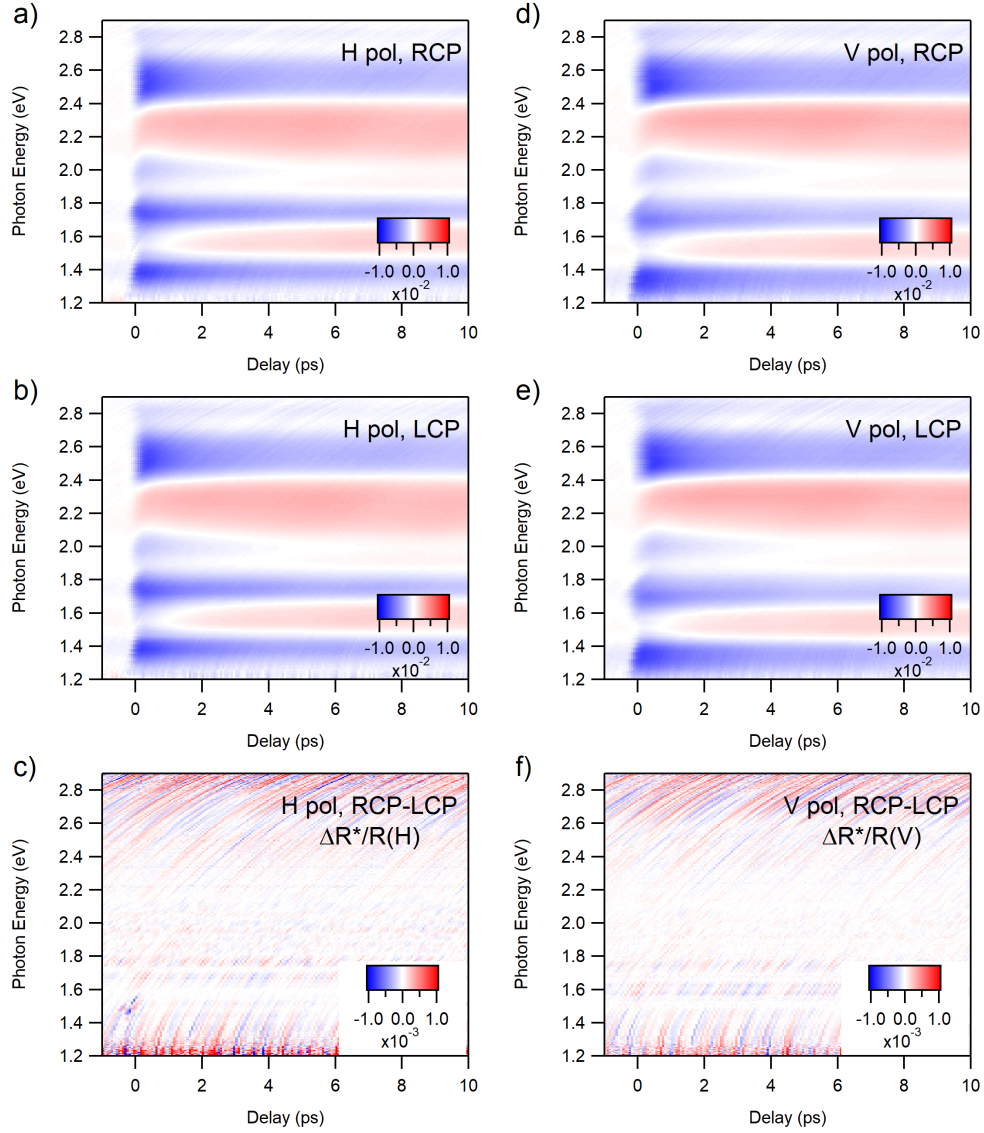


FIG. ED3. Differential reflectivity maps $\Delta R/R$ for bulk 2H-MoTe₂ with pump phonon energy at $\omega_{\text{pump}} = 1.55$ eV. Panels (a)-(b) show $\Delta R/R$ along the H direction for RCP and LCP, respectively, while panel (c) shows the dichroism $\Delta R^*/R = \Delta R/R_{\text{RCP}} - \Delta R/R_{\text{LCP}}$. The lack of dichroism in both the H and V directions point out the absence of Kerr rotation under these circumstances.